

Energy cascade with small-scales thermalization, counterflow metastability and anomalous velocity of vortex rings in Fourier-truncated Gross-Pitaevskii equation

Giorgio Krstulovic and Marc Brachet

*Laboratoire de Physique Statistique de l'Ecole Normale Supérieure,
associé au CNRS et aux Universités Paris VI et VII, 24 Rue Lhomond, 75231 Paris, France*
(Dated: April 2, 2022)

The statistical equilibria of the (conservative) dynamics of the Gross-Pitaevskii Equation (GPE) with a finite range of spatial Fourier modes are characterized using a new algorithm, based on a stochastically forced Ginzburg-Landau equation (SGLE), that directly generates grand canonical distributions. The SGLE-generated distributions are validated against finite-temperature GPE-thermalized states and exact (low-temperature) results obtained by steepest descent on the (grand canonical) partition function. A standard finite-temperature second-order λ -transition is exhibited.

A new mechanism of GPE thermalization through a direct cascade of energy is found using initial conditions with mass and energy distributed at large scales. A long transient with partial thermalization at small-scales is observed before the system reaches equilibrium. Vortices are shown to disappear as a prelude to final thermalization and their annihilation is related to the contraction of vortex rings due to mutual friction. Increasing the amount of dispersion at truncation wavenumber is shown to slowdown thermalization and vortex annihilation. A bottleneck that produces spontaneous effective self truncation with partial thermalization is characterized in the limit of large dispersive effects.

Metastable counter-flow states, with non-zero values of momentum, are generated using the SGLE algorithm. Spontaneous nucleation of vortex ring is observed and the corresponding Arrhenius law is characterized. Dynamical counter-flow effects on vortex evolution are investigated using two exact solutions of the GPE: traveling vortex rings and a motionless crystal-like lattice of vortex lines. Longitudinal effects are produced and measured on the crystal lattice. A dilatation of vortex rings is obtained for counter flows larger than their longitudinal velocity. The vortex ring longitudinal velocity has a dependence on temperature that is an order of magnitude above that of the crystal lattice, an effect that is related to the presence of finite-amplitude Kelvin waves. This anomalous vortex ring velocity is quantitatively reproduced by assuming equipartition of energy of the Kelvin waves. Orders of magnitude are given for the predicted effects in weakly interacting Bose-Einstein condensates and superfluid ^4He .

PACS numbers: 03.75.Kk, 05.30.Jp, 47.37.+q, 67.25.dk

I. INTRODUCTION

Finite temperature superfluids are typically described as a mixture of two interpenetrating fluids¹. At low temperatures the normal fluid can be neglected and Landau's two-fluids model reduces to the Euler equation for an ideal fluid that is irrotational except on (singular) vortex lines around which the circulation of the velocity is quantized. At finite temperature, when both normal fluid and superfluid vortices are present (e.g. in the counter-flow produced by a heat current) their interaction, called "mutual friction", must also be accounted for².

In the low-temperature regime the Gross-Pitaevskii equation (GPE) (also called the Nonlinear Schrödinger Equation) is an alternative description of superfluids and Bose-Einstein Condensates (BEC)³. The GPE is a partial differential equation (PDE) for a complex wave field that is related to the superflow's density and velocity by Madelung's transformation⁴. The (non singular) nodal lines of the complex wave field correspond to the quantum vortices that appear naturally in this model with the correct amount of velocity circulation. Just as the incompressible Euler equation, the GPE dynamics is known to produce⁵⁻⁸ an energy cascade that leads to a

Kolmogorov regime with an energy spectrum scaling as $E(k) \sim k^{-5/3}$. This Kolmogorov regime was also experimentally observed in low temperature helium^{9,10}. In this experimental context, note that so much progress has been made that it is now possible to visualize superfluid vortices both in the low-temperature regime and in the presence of counter flow by following the trajectories of solid hydrogen tracers in helium^{11,12}.

It has been suggested that the GPE should also be able to describe the classical equilibrium aspects of a finite-temperature homogeneous system of ultracold gases, provided that a projection (or truncation) on a finite number of Fourier modes is performed^{3,13}. Such classical truncated systems have a long history in the context of fluid mechanics. Indeed, if the (conservative) Euler equation is spectrally truncated, by keeping only a finite number of spatial Fourier harmonics, it is well known that it admits absolute equilibrium solutions with Gaussian statistics and equipartition of kinetic energy among all Fourier modes¹⁴⁻¹⁷.

Recently, a series of papers focused on the dynamics of convergence of the truncated Euler equation toward the absolute equilibrium. It was found that (long-lasting) transient are obtained that are able to mimic

(irreversible) viscous effects because of the presence of a “gas” of partially-thermalized high-wavenumber Fourier modes that generates (pseudo) dissipative effects^{18–23}.

The main goal of the present paper is to obtain and study finite temperature dissipative and counter flow effects by extending to the Fourier-truncated GPE the dynamical results that were obtained in the framework of the truncated Euler equation. We now give a short review of what is already known about the truncated GPE dynamics.

The Fourier truncated Gross-Pitaevskii equation was first introduced in the context of Bose condensation by Davis et al.¹³ as a description of the classical modes of a finite-temperature partially-condensed homogeneous Bose gas. They considered random initial data defined in Fourier space by modes with constant modulus and random phases up to some maximum wavenumber (determined by the energy). They found that, the numerical evolution of the truncated Gross-Pitaevskii equation reached (microcanonical) equilibrium and that a condensation transition of the equilibrium was obtained when the initial energy was varied.

The same condensation transition was later studied by Connaughton et al.²⁴ and interpreted as a condensation of classical nonlinear waves. Using a modified wave turbulence theory with ultraviolet cutoff, they argued that the transition to condensation should be subcritical. They found their theory in quantitative agreement with numerical integration of the GPE, using the same stochastic initial conditions than those of reference¹³. However, the authors later argued that, as weak turbulence theory is expected to breakdown nearby the transition to condensation, the subcritical nature of the transition predicted by their theory was not physical²⁵.

Berloff and Svistunov²⁶, starting from periodic initial conditions similar to those of Davis et al.¹³, used a finite-difference scheme (exactly conserving energy and particle number) to characterized the dynamical scenario of the relaxation toward equilibrium. Using the same finite-difference scheme, Berloff and Youd²⁷ then studied the dissipative dynamics of superfluid vortices at nonzero temperatures and observed a contraction of the vortex rings that followed a universal decay law.

Our main results are the followings. The classical absolute equilibrium of ideal fluids when generalized to GPE superfluids describes a standard^{28,29} second-order phase transition. Long transient with energy cascade and partial small-scales thermalization are present in the relaxation dynamics. Dynamical counter-flow effects on vortex evolution are naturally present in the system and the vortex ring have anomalous velocities caused by thermally excited Kelvin waves.

The paper is organized as follows: Section II is devoted to the basic theoretical background that is needed to account for the dynamics and thermalization of the Fourier truncated GPE.

In Sec. III, the thermodynamic equilibrium is explored. The microcanonical and grand canonical distributions

are numerically shown to be equivalent. Exact analytical expressions for the low-temperature thermodynamic functions are obtained. A standard second-order λ phase transition is exhibited at finite-temperature using the SGLE-generated grand canonical states.

In Sec. IV, the direct energy cascade is considered as a new mechanism for GPE thermalization. Using initial data with mass and energy distributed at large scales, a long transient with partial thermalization at small-scales is characterized. Vortex annihilation is observed to take place and is related to mutual friction effects. A bottleneck producing spontaneous self truncation with partial thermalization and a time-evolving effective truncation wavenumber is characterized in the limit of large dispersive effects at the maximum wavenumber of the simulation.

In Sec. V, the new SGLE algorithm is used to generate counter-flow states, with non-zero values of momentum, that are shown to be metastable under SGLE evolution. The spontaneous nucleation of vortex ring and the corresponding Arrhenius law are characterized. Dynamical counter-flow effects are investigated using vortex rings and straight vortex lines arranged in crystal-like patterns. An anomalous translational velocity of vortex ring is exhibited and is quantitatively related to the effect of thermally excited finite-amplitude Kelvin waves. Orders of magnitude are estimated for the corresponding effects in weakly interacting Bose-Einstein condensates and superfluid ⁴He.

Section VI is our conclusion. The numerical methods and low-temperature thermodynamic functions are described in an appendix.

II. THEORETICAL BACKGROUND

This section deals with basic facts needed to understand the dynamics and thermalization of the Fourier truncated GPE. We first recall in section IIA1 the (untruncated) GPE dynamics, its associated conserved quantities and the corresponding spectra; this material can be skipped by the reader already familiar with the GPE model of superflow^{4,6}. The Fourier truncated GPE, its thermodynamical limit and the different statistical ensembles are then defined.

The thermodynamics of the truncated system is introduced in section IIB using the microcanonical distribution. The canonical and grand canonical distributions are also used as they allow to directly label the equilibrium states by temperature and particle numbers.

A stochastically forced Ginzburg-Landau equation (SGLE) is considered in section IIC and shown to define a new algorithm that directly generates the grand canonical distributions.

A. Galerkin truncated Gross-Pitaevskii equation

1. Conservation laws and Galilean invariance of the GPE

Superfluids and Bose-Einstein condensates^{3,30} can be described at low temperature by the Gross-Pitaevskii equation (GPE) that is a partial differential equation (PDE) for the complex field ψ that reads

$$i\hbar \frac{\partial \psi}{\partial t} = -\frac{\hbar^2}{2m} \nabla^2 \psi + g|\psi|^2 \psi, \quad (1)$$

where $|\psi|^2$ is the number of particles per unit volume, m is the mass of the condensed particles and $g = \frac{4\pi\hbar^2}{m}$, with \tilde{a} the s -wave scattering length. This equation conserves the Hamiltonian H , the total number of particles N and the momentum \mathbf{P} defined in volume V by

$$H = \int_V d^3x \left(\frac{\hbar^2}{2m} |\nabla \psi|^2 + \frac{g}{2} |\psi|^4 \right) \quad (2)$$

$$N = \int_V |\psi|^2 d^3x \quad (3)$$

$$\mathbf{P} = \int_V \frac{i\hbar}{2} (\psi \nabla \bar{\psi} - \bar{\psi} \nabla \psi) d^3x. \quad (4)$$

It will be useful for the next sections to explicitly write the conservation law of the momentum $\partial_t \frac{i\hbar}{2} (\psi \partial_j \bar{\psi} - \bar{\psi} \partial_j \psi) + \partial_k \Pi_{kj} = 0$, where the momentum flux tensor Π_{kj} is defined as⁶

$$\Pi_{kj} = \frac{\hbar^2}{2m} (\partial_k \bar{\psi} \partial_j \psi + \partial_k \psi \partial_j \bar{\psi}) + \delta_{kj} \left(\frac{g}{2} |\psi|^4 - \frac{\hbar^2}{4m} \nabla^2 |\psi|^2 \right). \quad (5)$$

It is well known that the GPE (1) can be mapped into hydrodynamics equations of motion for a compressible irrotational fluids using the Madelung transformation defined by

$$\psi(\mathbf{x}, t) = \sqrt{\frac{\rho(\mathbf{x}, t)}{m}} \exp \left[i \frac{m}{\hbar} \phi(\mathbf{x}, t) \right], \quad (6)$$

where $\rho(\mathbf{x}, t)$ is the fluid density and $\phi(\mathbf{x}, t)$ is the velocity potential such that $\mathbf{v} = \nabla \phi$. The Madelung transformation (6) is singular on the zeros of ψ . As two conditions are required (both real and imaginary part of ψ must vanish) these singularities generally take place on points in two-dimension and on curves in three-dimensions. The Onsager-Feynman quantum of velocity circulation around vortex lines $\psi = 0$ is given by h/m .

When eq.(1) is linearized around a constant $\psi = A_0$, the sound velocity is given by $c = \sqrt{g|A_0|^2/m}$ with dispersive effects taking place for length scales smaller than the coherence length defined by

$$\xi = \sqrt{\hbar^2/2m|A_0|^2g}. \quad (7)$$

ξ is also the length scale of the vortex core^{3,6}.

Following reference⁵ we define the total energy per unit volume $e_{\text{tot}} = (H - \mu N)/V - \mu^2/2g$ where μ is the chemical potential (see section II B). Using the hydrodynamical variables, e_{tot} can be written as the sum of three parts: the kinetic energy e_{kin} , the internal energy e_{int} and the quantum energy e_q defined by

$$e_{\text{kin}} = \frac{1}{V} \int d^3x \frac{1}{2} (\sqrt{\rho} \mathbf{v})^2 \quad (8)$$

$$e_{\text{int}} = \frac{1}{V} \int d^3x \frac{g}{2m^2} \left(\rho - \frac{\mu m}{g} \right)^2 \quad (9)$$

$$e_q = \frac{1}{V} \int d^3x \frac{\hbar^2}{2m^2} (\nabla \sqrt{\rho})^2. \quad (10)$$

Using Parseval's theorem, one can define corresponding energy spectra: e.g. the kinetic energy spectrum $e_{\text{kin}}(k)$ is defined as the sum over the angles of $\left| \frac{1}{(2\pi)^3} \int d^3r e^{ir_j k_j} \sqrt{\rho} v_j \right|^2$. e_{kin} can be further decomposed into compressible e_{kin}^c and incompressible e_{kin}^i , using $\sqrt{\rho} \mathbf{v} = (\sqrt{\rho} \mathbf{v})^c + (\sqrt{\rho} \mathbf{v})^i$ with $\nabla \cdot (\sqrt{\rho} \mathbf{v})^i = 0$ (see⁶ for details).

Finally note that the GPE (1) is invariant under the Galilean transformation

$$\psi'(\mathbf{x}, t) = \psi(\mathbf{x} - \mathbf{v}_G t, t) \exp \left\{ \frac{im}{\hbar} \left[\mathbf{v}_G \cdot \mathbf{x} - \frac{1}{2} v_G^2 t \right] \right\}. \quad (11)$$

Under this transformation eqs.(2-4) transform as

$$H' = \frac{1}{2} m N v_G^2 + \mathbf{P} \cdot \mathbf{v}_G + H \quad (12)$$

$$N' = N \quad (13)$$

$$\mathbf{P}' = m N \mathbf{v}_G + \mathbf{P}. \quad (14)$$

2. Definition of the Fourier truncated GPE

For a periodical $3d$ system of volume V the Fourier truncated GPE is defined by performing a Galerkin truncation that consists in keeping only the Fourier modes with wavenumbers smaller than a UV cut-off k_{max} .

Expressing ψ in terms of the Fourier modes $A_{\mathbf{k}}$ as

$$\psi(\mathbf{x}, t) = \sum_{\mathbf{k}} A_{\mathbf{k}}(t) e^{i\mathbf{k} \cdot \mathbf{x}}, \text{ with } \frac{\mathbf{k}}{k_{\text{min}}} \in \mathbb{Z}^3, \quad (15)$$

and where $k_{\text{min}} = 2\pi/V^{1/3}$ is the smallest wavenumber. The Galerkin (Fourier) truncated Gross-Pitaevskii equation (TGPE) is defined as

$$-i\hbar \frac{\partial A_{\mathbf{k}}}{\partial t} = -\frac{\hbar^2 k^2}{2m} A_{\mathbf{k}} - \sum_{\mathbf{k}_1, \mathbf{k}_2} A_{\mathbf{k}_1} A_{\mathbf{k}_2 + \mathbf{k}_1}^* A_{\mathbf{k} + \mathbf{k}_2}, \quad (16)$$

where the Fourier modes satisfy $A_{\mathbf{k}} = 0$ if $k \geq k_{\text{max}}$ and the sum is performed over all wavenumbers satisfying $|\mathbf{k}_1|, |\mathbf{k}_2|, |\mathbf{k}_2 + \mathbf{k}_1|, |\mathbf{k} + \mathbf{k}_2| < k_{\text{max}}$. This time-reversible finite system of ordinary differential equations with a large number of degree of freedom $\mathcal{N} \sim$

$(k_{\max}/k_{\min})^3$ also conserves the energy, number of particles and momentum.

The direct numerical evolution of the convolution in eq.(16) would be very expensive in computational time $O(N^6)$, where N is the resolution. This difficulty is avoided by using pseudo-spectral methods³¹ and the non-linear term is calculated in physical space, using FFTs that reduce the CPU time to $O(N^3 \log N)$. Introducing the Galerkin projector \mathcal{P} that reads in Fourier space $\mathcal{P}_G[A_{\mathbf{k}}] = \theta(k_{\max} - k)A_{\mathbf{k}}$ with $\theta(\cdot)$ the Heavside function, the TGPE (16) can be written as

$$i\hbar \frac{\partial \psi}{\partial t} = \mathcal{P}_G \left[-\frac{\hbar^2}{2m} \nabla^2 \psi + g \mathcal{P}_G[|\psi|^2] \psi \right]. \quad (17)$$

Equation (17) exactly conserves energy and mass and, if it is correctly de-aliased using the 2/3-rule³¹ (dealiasing at $k_{\max} = \frac{2}{3} \frac{N}{2}$), it also conserves momentum (see Appendix A for a explicit demonstration). The Galerkin truncation also preserves the Hamiltonian structure with the truncated Hamiltonian $H = \int d^3x \left(\frac{\hbar^2}{2m} |\nabla \psi|^2 + \frac{g}{2} [\mathcal{P}_G|\psi|^2]^2 \right)$.

Let us remark that perhaps a more standard definition of dealiasing in eq.(17) could have been $\mathcal{P}_G[|\psi|^2 \psi]$ using 1/2-rule (dealiasing at $k_{\max} = \frac{1}{2} \frac{N}{2}$) rather than $\mathcal{P}_G[\mathcal{P}_G[|\psi|^2] \psi]$ with the 2/3-rule. Using the former definition there is no restriction $|\mathbf{k}_2| < k_{\max}$ on the convolution in eq.(16). Both methods are equivalent in the partial differential equation (PDE) limit (exponential decay of energy spectrum for $k \ll k_{\max}$) and admit the same invariants. However the scheme of eq.(17) is preferable because k_{\max} is larger at the same resolution. If dealiasing is not preformed in equation (17) the errors in the conservation of momentum can rise up to 50% in a few units of time (see Appendix A). In a finite difference scheme the conservation of momentum should also be checked carefully as it is bound to produce spurious effects.

Another effect caused by periodic boundary condition is that the velocity \mathbf{v}_G in the Galilean transformation (11) is quantized by the relation

$$\mathbf{v}_G = \frac{\hbar}{m} \frac{2\pi}{V^{1/3}} \mathbf{n}_G, \quad (18)$$

where $\mathbf{n}_G \in \mathbb{Z}^3$ and \mathbf{v}_s becomes continuous only in the limit $\hbar/(mV^{1/3}) \rightarrow 0$. The Galilean invariance is slightly broken by the TGPE (16) because of modes close to the truncation wavenumber k_{\max} . However it is recovered in the PDE limit where high wavenumber modes are converging exponentially and also in the thermodynamic limit: $\frac{k_{\max}}{k_{\min}} \rightarrow \infty$ defined below because the offending terms represent only a surface effect in Fourier space.

3. Thermodynamical limit and statistical ensembles

Let us first notice that the energy H , the number of particles N and the momentum \mathbf{P} in eqs. (2-4) are all proportional to the total number of modes $\mathcal{N} \sim k_{\max}^3 V$

and therefore are all extensive quantities. Also note that by definition of the coherence length (7), the number ξk_{\max} determines the amount of dispersion at truncation wavenumber in the system.

The thermodynamic limit $V \rightarrow \infty$ of the truncated Gross-Pitaevskii system is thus defined as the limit

$$\mathcal{N} \rightarrow \infty, \quad \xi k_{\max} = \text{constant}, \quad (19)$$

in order to obtain equivalent systems. In this limit the relevant thermodynamic variables are the intensive quantities H/V , N/V and \mathbf{P}/V . In practice, to perform numerical computations we will fix the volume to $V = (2\pi)^3$ and we will vary k_{\max} (see paragraphs before section III).

Let us define, as usual the microcanonical ensemble³² by the probability dw of finding the system in states with given values of energy H_{in} , number of particles N_{in} (the subscript “in” stands for initial data) and momentum \mathbf{P}_{in} given by:

$$dw = \text{cte } e^S \delta(H - H_{\text{in}}) \delta(N - N_{\text{in}}) \delta^3(\mathbf{P} - \mathbf{P}_{\text{in}}) dH dN d^3P, \quad (20)$$

where $S = \log \Gamma$ is the entropy with Γ the number of accessible micro-states.

Microcanonical statistical states can be obtained numerically by time-integrating the TGPE until the system reaches thermodynamic equilibrium^{13,24}. These thermalized states are formally determined by the control values H_{in} , N_{in} and \mathbf{P}_{in} that are set in the initial condition. It has been shown in references^{13,24} by varying the values of H_{in} that TGPE present a phase transition analogous to the one of Bose-Einstein condensation, where the 0-wave-number A_0 vanish for finite values of H_{in} . Note that an explicit expression of dw or S cannot be easily obtained in the microcanonical ensemble and therefore the temperature is not easily accessible.

A simple way to explicitly control the temperature is to use the canonical or grand canonical formulation. The grand canonical distribution probability is given by a Boltzman weight

$$\mathbb{P}_{\text{st}} = \frac{1}{\mathcal{Z}} e^{-\beta F} \quad (21)$$

$$F = H - \mu N - \mathbf{W} \cdot \mathbf{P}, \quad (22)$$

where \mathcal{Z} is the grand partition function, β is the inverse temperature and μ is the chemical potential. In what follows we will refer to \mathbf{W} as the counterflow velocity.

Note that when $\mathbf{W} = 0$, $F = H - \mu N$ and the statistic weight of distribution (21) corresponds to the $\lambda - \phi^4$ theory studied in second order phase transitions^{28,29}. This point will be further discussed in subsection III C.

Finally remark that the states with $\mathbf{W} \neq 0$ are obtained, in the thermodynamic limit, by a Galilean transformation of the basic $\mathbf{W} = 0$ state (see below eq. (71)). However, for finite size systems, because of the quantification of the Galilean transformation (eqs.(11) and (18)) new metastable states with counterflow appear. These metastable states and their interactions with vortices will be studied in detail below in section V A.

In the grand canonical ensemble (21-22) the mean energy \bar{H} , number of particles \bar{N} and momentum $\bar{\mathbf{P}}$ are easily obtained by defining the grand canonical potential

$$\Omega = -\beta^{-1} \log \mathcal{Z} \quad (23)$$

and using the relations

$$\bar{N} = -\frac{\partial \Omega}{\partial \mu}, \quad \bar{\mathbf{P}} = -\frac{\partial \Omega}{\partial \mathbf{P}}, \quad \bar{H} = \frac{\partial \Omega}{\partial \beta} + \mu \bar{N} + \mathbf{W} \cdot \bar{\mathbf{P}}. \quad (24)$$

Observe that the microcanonical states (20) are characterized by the values H_{in} , N_{in} and \mathbf{P}_{in} . On the other hand, the grand canonical states are controlled by the conjugate variables: β , μ and \mathbf{W} . The different statistical ensembles are expected to be equivalent in the thermodynamics limit (19) and therefore

$$H_{\text{in}} = \bar{H}, \quad N_{\text{in}} = \bar{N}, \quad \mathbf{P}_{\text{in}} = \bar{\mathbf{P}}, \quad (25)$$

in this limit. The equivalence of ensembles will be numerically tested below in subsection III A.

In the grand canonical ensemble, the pressure p is usually defined from the grand canonical potential (23) by the relation³² $\Omega = -pV$. This definition presents two problems in the TGPE system. First, due to classical statistics Ω has a logarithmic divergence at $\beta = \infty$. Second, this definition does not coincide with the standard relation in fluid dynamics involving the diagonal part of the momentum flux tensor Π_{ij} (see eq.(5)). Both these problems can be solved by considering the total number of modes as a new thermodynamics variable, as we will see in the next section.

B. Thermodynamics of truncated system

When a Galerkin truncation is performed on a system a new variable k_{max} explicitly appears. One thus find that the thermodynamic potentials depend on the total number of modes. Denoting $\lambda_{\mathcal{N}}$ the conjugate variable to the total number of modes \mathcal{N} the standard thermodynamic relation for the energy easily generalizes as

$$dE = -pdV + TdS + \mu dN + \lambda_{\mathcal{N}} d\mathcal{N} + \mathbf{W} \cdot d\mathbf{P} \quad (26)$$

with S the entropy and where we have included the total momentum dependence $d\mathbf{P}$. As in Landau two-fluid model¹ eq. (26) is written in a system of reference where $\mathbf{v}_s = \overline{\nabla \phi} = \mathbf{0}$ (the bar standing for some ensemble average) and $E = \bar{H}$ is the macroscopic energy.⁶¹ We will omit the bar over the others microscopic quantities. Note that the Fourier modes formally play the role of “particles” and $\lambda_{\mathcal{N}}$ is formally the “chemical potential” associated to those “particles”.

The thermodynamic potentials can be easily generalized to take in to account the new variables. It is useful to define the Gibbs potential G , grand canonical Ω and

a generalized grand canonical potential Ω' (with a Legendre transformation on \mathcal{N}) as

$$G = E - TS + pV - \mathbf{W} \cdot \mathbf{P} \quad (27)$$

$$\Omega = E - TS - \mu N - \mathbf{W} \cdot \mathbf{P} \quad (28)$$

$$\Omega' = E - TS - \mu N - \lambda_{\mathcal{N}} \mathcal{N} - \mathbf{W} \cdot \mathbf{P} \quad (29)$$

from where their respective variations follows:

$$dG = Vdp - SdT + \mu dN + \lambda_{\mathcal{N}} d\mathcal{N} - \mathbf{P} \cdot d\mathbf{W} \quad (30)$$

$$d\Omega = -pdV - SdT - N d\mu + \lambda_{\mathcal{N}} d\mathcal{N} - \mathbf{P} \cdot d\mathbf{W} \quad (31)$$

$$d\Omega' = -pdV - SdT - N d\mu - \mathcal{N} d\lambda_{\mathcal{N}} - \mathbf{P} \cdot d\mathbf{W} \quad (32)$$

Based on standard arguments of extensive variables³² and noting that $\lambda_{\mathcal{N}}$ and \mathbf{W} are intensive variables we find the standard formula of the Gibbs potential with two types of particles

$$G = \mu N + \lambda_{\mathcal{N}} \mathcal{N}. \quad (33)$$

Using eqs.(27) and (33) in eqs.(28) and (29) we find

$$\Omega = -pV + \lambda_{\mathcal{N}} \mathcal{N}, \quad \Omega' = -pV \quad (34)$$

The relations (26-34) determine all the thermodynamic variables and potentials. For instance the pressure p can be obtained from eq.(31), eq.(32) or eq.(34) by

$$p = -\left. \frac{\partial \Omega}{\partial V} \right|_{T, \mu, \mathcal{N}, \mathbf{W}} = -\frac{\Omega - \lambda_{\mathcal{N}} \mathcal{N}}{V} = -\frac{\Omega'}{V} \quad (35)$$

where $\lambda_{\mathcal{N}} = \left. \frac{\partial \Omega}{\partial \mathcal{N}} \right|_{V, T, \mu, \mathbf{W}}$.

We proceed now to show that thermodynamic definition (35) of the pressure coincides with the standard relation in fluid dynamics. In order to make explicit the dependence of the energy H on the volume V let us define the dimensionless space variables $\tilde{x} = x/V^{1/3}$ and $\tilde{\psi} = V^{1/2}\psi$. Expressed in term of these variables the Hamiltonian (2) reads $H = \int d^3\tilde{x} \left(\frac{\hbar^2}{2m} \frac{1}{V^{2/3}} |\tilde{\nabla} \tilde{\psi}|^2 + \frac{1}{V} \frac{g}{2} |\tilde{\psi}|^4 \right)$. Taking the derivative with respect to V and reintroducing x and ψ yields

$$\frac{\partial H}{\partial V} = -\frac{1}{V} \int d^3x \left(\frac{\hbar^2}{2m} \frac{2}{3} |\nabla \psi|^2 + \frac{g}{2} |\psi|^4 \right). \quad (36)$$

This expression corresponds to the spatial average of the the diagonal part of Π_{ik} . As by definition $E = \bar{H}$ and the derivative has been implicitly done at constant total number of modes and momentum we find, using the thermodynamic relation (26) and eq.(36), that the pressure satisfies

$$p = -\left. \frac{\partial E}{\partial V} \right|_{S, N, \mathcal{N}, \mathbf{P}} = -\left. \frac{\partial \bar{H}}{\partial V} \right|_{N, \mathcal{N}, \mathbf{P}}, \quad (37)$$

where the second equality holds for adiabatic compressions³².

Finally by replacing Ω in eq.(28) we obtain the thermodynamic relation

$$E + pV - \mu N - \mathbf{W} \cdot \mathbf{P} = TS + \lambda_{\mathcal{N}} \mathcal{N}. \quad (38)$$

Let us remark that, in a classical system, the entropy is defined up to an additive constant related to the normalization of the phase-space. However the quantity $TS + \lambda_{\mathcal{N}} \mathcal{N}$ is completely determined because each term in the left hand side of eq.(38) is well defined. By the same arguments $d(\mathcal{N} \lambda_{\mathcal{N}}/T)$ is also a completely determined quantity. If the variable \mathcal{N} had not been taken into account, the corresponding pressure would be $-\Omega/V$ and therefore wrongly defined and depending on the normalization constant. The grand canonical potential Ω will be explicitly obtained at low-temperature in subsection IIIB where the above considerations can be explicitly checked.

C. Generation of grand canonical distribution using a stochastic Ginzburg-Landau equation

Grand canonical equilibrium states given by the statistics (21-22) cannot be easily obtained because the Hamiltonian H in eq.(2) is not quadratic and therefore the statistical distribution is not Gaussian. Nevertheless it is possible to construct a stochastic process that converges to a stationary solution with equilibrium distribution (21-22). This process is defined by a Langevin equation consisting of a stochastic Ginzburg-Landau equation (SGLE) that reads

$$\hbar \frac{\partial A_{\mathbf{k}}}{\partial t} = -\frac{1}{V} \frac{\partial F}{\partial A_{\mathbf{k}}^*} + \sqrt{\frac{2\hbar}{V\beta}} \hat{\zeta}(\mathbf{k}, t) \quad (39)$$

$$\langle \zeta(\mathbf{x}, t) \zeta^*(\mathbf{x}', t') \rangle = \delta(t - t') \delta(\mathbf{x} - \mathbf{x}'), \quad (40)$$

where F is defined in eq.(22) and $\hat{\zeta}(\mathbf{k}, t)$ is the (k_{\max} -truncated) Fourier transform of the gaussian white-noise $\zeta(\mathbf{x}, t)$ defined by eq.(40). The Langevin equation (39-40) explicitly reads in physical space

$$\begin{aligned} \hbar \frac{\partial \psi}{\partial t} = & \mathcal{P}_{\mathbf{G}} \left[\frac{\hbar^2}{2m} \nabla^2 \psi + \mu \psi - g \mathcal{P}_{\mathbf{G}}[|\psi|^2] \psi - i \hbar \mathbf{W} \cdot \nabla \psi \right] \\ & + \sqrt{\frac{2\hbar}{V\beta}} \mathcal{P}_{\mathbf{G}}[\zeta(\mathbf{x}, t)]. \end{aligned} \quad (41)$$

In the $T \rightarrow 0$ limit eq.(41) reduce to the advective real Ginzburg-Landau equation (up to a redefinition of μ) that was introduced in reference⁶. This equation has the same stationary solutions of than the TGPE (17) in a system of reference moving with velocity \mathbf{W} . When also included in the TGPE the term $\mu \psi$ in eq.(41) has, because of particle number conservation, the only effect of adding a global time-dependent phase factor to the solution.

The probability distribution $\mathbb{P}[\{A_{\mathbf{k}}, A_{\mathbf{k}}^*\}_{\mathbf{k} < k_{\max}}]$ of the stochastic process defined by eqs.(39-40) can be shown

to obey the following Fokker-Planck equation^{33,34}

$$\frac{\partial \mathbb{P}}{\partial t} = \sum_{\mathbf{k} < k_{\max}} \frac{\partial}{\partial A_{\mathbf{k}}} \left[\frac{1}{V\hbar} \frac{\partial F}{\partial A_{\mathbf{k}}^*} \mathbb{P} + \frac{1}{V\hbar\beta} \frac{\partial \mathbb{P}}{\partial A_{\mathbf{k}}^*} \right] + c.c. \quad (42)$$

It is straightforward to demonstrate that the probability distribution (21) is a stationary solution of eq.(42), provided that βF is a positive defined function of $\{A_{\mathbf{k}}, A_{\mathbf{k}}^*\}_{\mathbf{k} < k_{\max}}$.

In order to directly control the value of the number of particles or the pressure, the SGLE must be supplied with one of two *ad-hoc* equation for the chemical potential. These equation simply read

$$\frac{d\mu}{dt} = -\nu_N (N - N^*)/V \quad (43)$$

$$\frac{d\mu}{dt} = -\nu_p (p - p^*) \quad (44)$$

where the pressure p is computed as $p = -\frac{\partial H}{\partial V}$ (see eq.(36)). Equation (43) controls the number of particles and fixes its mean value to the control value N^* . Similarly eq.(44) controls the pressure and fixes its value at p^* . Equations (43-44) are not compatible and they must not be used simultaneously. Depending on the type of the temperature scans, the SGLE must be used together with either eq.(43), eq.(44) or solely with a fixed value of μ .

In the rest of this paper we will perform several numerical simulations of the TGPE (16) and SGLE (41). For numerics, the parameters in SGLE (omitting the Galerkin projector \mathcal{P}) will be rewritten as

$$\frac{\partial \psi}{\partial t} = \alpha \nabla^2 \psi + \Omega'_0 \psi - \beta_0 |\psi|^2 \psi - i \mathbf{W} \cdot \nabla \psi + \sqrt{\frac{k_B T}{\alpha}} \zeta,$$

with similar changes for TGPE.

In terms of α , Ω'_0 and β_0 the physical relevant parameters are the coherence length ξ and the velocity of sound c defined in section II A 1 (eq.(7) and text before). They can be expressed as

$$\xi = \sqrt{\alpha/\Omega'_0}, \quad c = \sqrt{2\alpha\beta_0\rho^*} \quad (45)$$

with $\rho^* = \Omega'_0/\beta_0$. The value of the density at $T = 0$ set to $\rho^* = 1$ in all the simulations presented below. In order to keep the value of intensive variables constant in the thermodynamic limit (19), with V constant and $k_{\max} \rightarrow \infty$ the inverse temperature is expressed as $\beta = 1/k_{\mathcal{N}} T$ where $k_{\mathcal{N}} = V/\mathcal{N}$. With these definitions the temperature T has units of energy per volume and $4\pi\alpha$ is the quantum of circulation.

With ξ fixed, the value of ξ/c only determine a time-scale. The velocity of sound is set to $c = 2$ and the different runs presented below are obtained by varying only the coherence length ξ , the temperature T , the counter-flow velocity \mathbf{W} and the UV cut-off wavenumber k_{\max} . The number ξk_{\max} is kept constant when the resolution

is changed, except in section IV B where dispersive effects are studied. Finally in all numerical results the energy and momentum are presented per unit of volume $V = (2\pi)^3$ and the control values of number of particles and pressure in eqs.(43-44) are set to $mN^*/V = \rho^* = 1$ and $p^* = c^2\rho^{*2}/2 = 2$. Numerical integration are performed by using periodic pseudo-spectral codes and the time-stepping schemes are Runge-Kutta of order 4 for TGPE and implicit Euler for SGLE.

III. CHARACTERIZATION OF THERMODYNAMIC EQUILIBRIUM

In this section, the thermodynamic equilibrium is explored and characterized. The microcanonical and grand canonical distributions are first shown to be numerically equivalent in a range of temperatures by comparing the statistics of GPE and SGLE generated states in section III A. The steepest descent method is then applied to the grand partition function in section III B to obtain exact analytical expressions for the low-temperature thermodynamic functions. The basic numerical tools are validated by reproducing these low-temperature results. In section III C a standard second-order λ phase transition is exhibited at finite-temperature using the SGLE-generated grand canonical states and the deviations to low-temperature equipartition are characterized.

A. Comparison of microcanonical and grand canonical states

We now numerically compare the statistics of the grand canonical states produced by the new algorithm SGLE to the statistics of the microcanonical states obtained by long-time integrations of TGPE. The coherence length is set to $\xi = \sqrt{2}/10$ and 32^3 collocation points are used ($k_{\max} = 10$). The initial condition for the TGPE runs are chosen with random phases in a similar way than in references^{13,24}. We obtain low, medium and high values of the energy with constant density $\rho = mN/V = 1$ (see table I).

TABLE I: Parameters of TGPE initial condition and time steps.

H	T	TGPE time steps	SGLE time steps
0.09	0.09	40000	9600
0.5	0.5	20000	9600
1.96	1.8	20000	9600
4.68	4	20000	5000

To compare with the SGLE generated statistics a scan in temperature at constant density $\rho = 1$ is performed in order to obtain the temperature corresponding to the

energies of the TGPE runs. Using the thermalized final states obtained from TGPE and converged final states of SGLE histograms of the density $\rho(x)$ in physical space are confronted in Fig.1. They are found to be in excellent agreement.

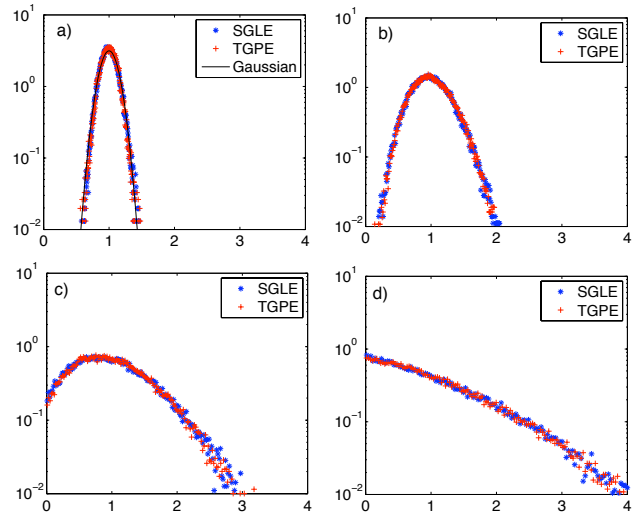


FIG. 1: Comparison of density histograms obtained by SGLE and TGPE dynamics ($\xi = 2/10\sqrt{2}$ and resolution 32^3) with energy equal to a) $H = 0.09$, b) $H = 0.51$, c) $H = 1.96$ and d) $H = 4.68$ (see table I). The solid line in a) is a Gaussian of standard deviation $\delta\rho^2 = 0.016$ (see below eq.(59)) computed with the low-temperature calculations of section III B.

Note that when the energy (or temperature) increases more weight becomes apparent on the histograms near $\rho = 0$, indicating the presence of vortices. The Gaussian character of the histogram in Fig. 1 a motivates the low-temperature calculation of the next section.

The SGLE converges much faster than the TGPE as apparent in table I. Because of the accurate conservative temporal scheme needed for the integration of the TGPE, the SGLE yields a large economy of the CPU time needed to reach equilibrium. On the local machines where these computations were performed the SGLE was typically more than 10 times faster than TGPE. Finally observe that, even at this relatively low 32^3 resolution, the thermodynamic limit has been reached in the sense that the micro and grand canonical distribution coincides.

B. Low-temperature calculation

The gaussian histogram of Fig.1.a strongly suggest that some quadratic approximation should be able to obtain exact analytical expressions for the thermodynamic functions at low temperature. In this section we use such an approximation to compute the grand partition function \mathcal{Z} and the grand canonical potential⁶² $\Omega = -\beta^{-1} \log \mathcal{Z}$ defined in (28).

The first step is to express the energy F of eq.(22) in terms of the Fourier amplitudes $A_{\mathbf{k}}$. This leads to a non quadratic function $F[A_{\mathbf{k}}, A_{\mathbf{k}}^*]$ explicitly given in appendix B (eqs.B1-B3). The grand partition function is a product integral over all the Fourier amplitudes

$$\mathcal{Z}(\beta, \mu, \mathbf{W}) = V^{\mathcal{N}} \int \frac{dA_0 dA_0^*}{2\pi} \prod_{\mathbf{k} < \mathbf{k}_{\max}} \frac{dA_{\mathbf{k}} dA_{\mathbf{k}}^*}{2\pi} e^{-\beta F[A_{\mathbf{k}}, A_{\mathbf{k}}^*]}. \quad (46)$$

The integrals in (46) cannot be done explicitly, however it is possible to give a low-temperature approximation using the method of *steepest descent*^{28,35}. In addition to F an *external field* $-\mu_0|A_0|^2V$ will be added in order to explicitly obtain the mean value of condensate Fourier mode $|A_0|^2$ by direct differentiation. The physical partition function is obtained by setting $\mu_0 = 0$. The integrals are dominated by the saddle-point determined by $\frac{\partial F}{\partial A_{\mathbf{k}}^*} - \mu_0 A_0 V \delta_{\mathbf{k}, \mathbf{0}} = 0$ that gives the solution (see eqs.(B4) and (B5))

$$g|A_0|^2|_{\text{sp}} = \mu + \mu_0 \quad A_{\mathbf{k}} = 0 \text{ for } \mathbf{k} \neq \mathbf{0}, \quad (47)$$

where the subscript “sp” stands for saddle-point. Note that in general $|A_0|^2 \neq |A_0|^2|_{\text{sp}}$ and the mean value is equal to the saddle-point one only at $T = 0$. Other solutions that can be obtained when $\mathbf{W} \neq 0$ will be discussed in detail in section V.

In the saddle-point $A_{\mathbf{k}} = 0$ for $\mathbf{k} \neq \mathbf{0}$, we thus need to keep only quadratic terms in $A_{\mathbf{k}}$ to obtain the low-temperature approximation. Denoting $\mathbf{p} = \hbar\mathbf{k}$, at leading order F can be rewritten as $F = F_0 + F_1 + F_2$ with

$$F_0 = V \left(\frac{g}{2} |A_0|^4 - \mu |A_0|^2 \right) \quad (48)$$

$$F_1 = V \sum_{\mathbf{p} \neq \mathbf{0}} \left(\frac{p^2}{2m} - \mu + 2g|A_0|^2 - \mathbf{W} \cdot \mathbf{p} \right) |A_{\mathbf{p}}|^2 \quad (49)$$

$$F_2 = V \frac{g}{2} \sum_{\mathbf{p} \neq \mathbf{0}} A_{\mathbf{0}}^* A_{\mathbf{p}} A_{-\mathbf{p}} + A_{\mathbf{0}}^2 A_{\mathbf{p}}^* A_{-\mathbf{p}}^*. \quad (50)$$

To obtain the low-temperature partition function we must compute the determinant of the matrix $\frac{\partial^2 F}{\partial A_{\mathbf{p}} \partial A_{\mathbf{q}}^*} - \mu_0 V \delta_{\mathbf{p}, \mathbf{0}} \delta_{\mathbf{q}, \mathbf{0}}$. This determinant can be obtained using the Bogoliubov transformation

$$A_{\mathbf{p}} = u_p B_{\mathbf{p}} + v_p B_{-\mathbf{p}}^* \quad (51)$$

with $u_p = \frac{A_0}{|A_0|} \frac{1}{\sqrt{1-L_p^2}}$, $v_p = \frac{A_0}{|A_0|} \frac{L_p}{\sqrt{1-L_p^2}}$ and where L_p is determined by imposing the diagonalization of $F - \mu_0|A_0|^2V$. L_p is explicitly given in eq.(B6). Is easy to show that (51) is a canonical transformation and the

normalization condition of the Poisson bracket implies $|u_p|^2 - |v_p|^2 = 1$.

Expressing F in the Bogoliubov basis we obtain

$$F = V \left[\frac{g}{2} |A_0|^4 - \mu |A_0|^2 + \sum_{\mathbf{p} \neq \mathbf{0}} (\epsilon(p; \mu, \mu_0) - \mathbf{W} \cdot \mathbf{p}) |B_{\mathbf{p}}|^2 \right] \quad (52)$$

with the dispersion relation (see appendix B)

$$\epsilon(p; \mu, \mu_0) = \sqrt{\left(\mu + 2\mu_0 + \frac{p^2}{2m} \right)^2 - (\mu + \mu_0)^2}. \quad (53)$$

The excited modes $B_{\mathbf{p}}$ are called phonons in quantum mechanics. Here, because of classical statistics and the quadratic Hamiltonian, there is equipartition among phonon modes. Replacing the value of the chemical potential by the saddle-point $\mu = g|A_0|^2|_{\text{sp}}$ (with $\mu_0 = 0$), eq.(53) yields the well known Bogoliubov dispersion relation³⁶. The Bogoliubov relation $\epsilon(p)$ can also be directly obtained from the GPE by expressing ψ in hydrodynamics variables, using the Madelung transformation (6) and linearizing around an homogenous density $\rho_0 = m|A_0|^2$.

The partition function now trivially factorizes in independent parts $\mathcal{Z}(\beta, V, \mu, \mathbf{W}, \mathcal{N}, \mu_0) = \mathcal{Z}_0(\beta, \mu, \mu_0) \prod_{\mathbf{p} \neq \mathbf{0}} \mathcal{Z}_{\mathbf{p}}(\beta, \mu, \mathbf{W}, \mu_0)$ where

$$\mathcal{Z}_0(\beta, V, \mu, \mu_0) = \sqrt{2\pi^3} \sqrt{\frac{V}{g\beta}} e^{\frac{V\beta(\mu+\mu_0)^2}{2g}} \quad (54)$$

$$\mathcal{Z}_{\mathbf{p}}(\beta, \mu, \mathbf{W}, \mu_0) = \frac{1}{\beta(\epsilon(p; \mu, \mu_0) - \mathbf{W} \cdot \mathbf{p})} \quad (55)$$

The total number of modes $\mathcal{N} = \sum_{\mathbf{k}} 1$ and the grand canonical potential Ω are sums over all wave-numbers

$$\Omega(\beta, V, \mu, \mathbf{W}, \mathcal{N}) = -\beta^{-1} \left[\log \mathcal{Z}_0 + \sum_{\mathbf{p} \neq \mathbf{0}} \log \mathcal{Z}_{\mathbf{p}} \right] \quad (56)$$

from where all thermodynamic quantities directly follows by using the thermodynamic relation (31).

Replacing the sum by an integral the expression for the number of modes reads

$$\mathcal{N} = \int_0^{P_{\max}} \frac{p^2 V}{2\pi^2 \hbar^3} dp = \frac{P_{\max}^3 V}{6\pi^2 \hbar^3}. \quad (57)$$

Setting $\mathbf{W} = (0, 0, w)$ the integral form of eq. (56) reads

$$\begin{aligned}
\Omega(\beta, V, \mu, w, \mathcal{N}) &= -\frac{V(\mu + \mu_0)^2}{2g} + \int_0^{P_{\max}} \int_{-1}^1 \frac{p^2 V}{2\pi^2 \hbar^3} \log \left(\beta \sqrt{\left(\mu + 2\mu_0 + \frac{p^2}{2m} \right)^2 - (\mu + \mu_0)^2} - \beta p w z \right) \frac{dz dp}{2} \\
&= -\frac{V(\mu + 2\mu_0)}{2g} - \frac{P_{\max}^3 V}{6\pi^2 \beta \hbar^3} \left\{ \frac{2}{3} - \log [\beta \epsilon(P_{\max}; \mu)] - f \left[\frac{4m\mu}{P_{\max}^2} \right] \left(1 - \frac{w^2 m}{2\mu} \right) - \frac{\mu_0}{\mu} f_0 \left[\frac{4m\mu}{P_{\max}^2} \right] \right\} \quad (58)
\end{aligned}$$

where in (58) the thermodynamic limit (19) of infinite volume⁶³ has been taken and the conditions $w^2 \ll \mu/m$, $\mu_0/\mu \ll 1$ have been used. The functions $f[z]$ and $f_0[z]$ are explicated in eqs.(B10-B11). Note that the dependence of the grand canonical potential Ω on the number of modes \mathcal{N} is implicitly given by P_{\max} and eq.(57). The first term in Ω is due to the condensated mode at $\mathbf{p} = 0$.

The low-temperature approximation to all thermodynamic functions is directly obtained from equation (58) by first setting $\mu_0 = 0$ and then differentiating (58), using relation (31). It is straightforward to check that both definition of the pressure in eq. (35) coincide. Furthermore the higher order moments of the density can be easily computed by taking successive derivatives of the grand canonical potential. For instance it is straightforward to show that the variance of the density ρ (see Fig.1.a) is given by

$$V^2\langle \delta \rho^2 \rangle = -\beta^{-1} m^2 \frac{\partial^2 \Omega}{\partial \mu^2}. \quad (59)$$

It can also be checked on the explicit expression for the entropy S (see eqs.(B9)) that, as expected for a classical system, the entropy depends by a logarithmic term on the phase-space normalization. However the function $TS + \lambda_{\mathcal{N}} \mathcal{N}$ is independent of phase-space normalization (see discussion below eq.(38)).

Finally, low-temperature expressions for the energies (8-10) and their corresponding spectra can be easily obtained using Madelung transformation (6). At low temperatures the fluctuations are small and e_{kin} depends only on ϕ and $e_q + e_{\text{int}}$ only on ρ . The total energy is thus decomposed in two non-interacting terms. Equipartition of energy between the total kinetic energy e_{kin} and quantum plus internal energy $e_q + e_{\text{int}}$ is thus expected at low temperature.

The next subsections will be concerned with the vanishing counterflow case $w = 0$. The states with non-zero counterflow w will be studied in details in section V.

C. λ transition and vortices

To characterize the condensation transition, we present here four temperature scans performed using SGLE (41). Three of them are at resolution of 64^3 with respectively constant chemical potential, density and pressure (using eqs.(43-44)). The fourth scan is performed at con-

stant pressure but at a resolution of 128^3 . The coherence length is fixed so that $\xi k_{\max} = 1.48$ is kept constant.

Figure 2.a displays the results of the scans. Observe that the behavior at low-temperature is in good agreement with the low-temperature analytical calculations of section IIIB and the explicit formulae given in appendix B. Also note that the constant pressure scans at resolutions of 64^3 and 128^2 coincide for all temperatures showing that the thermodynamic limit (19) discussed in section IIB is obtained at these resolutions.

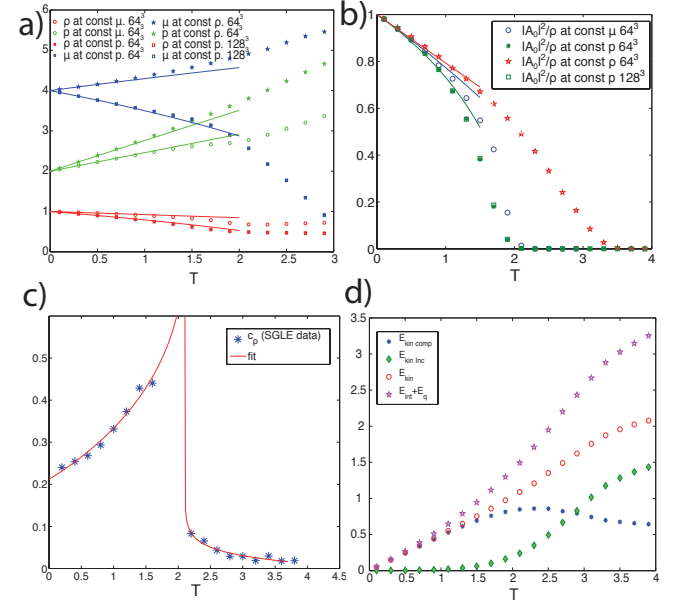


FIG. 2: a) Temperature dependence of the density ρ , pressure p and chemical potential μ for SGLE scans at constant density, pressure and chemical potential (see legend on figure). b) Temperature dependence of the condensate fraction $|A_0|^2/\rho$ (same scans as in a)). c) Specific heat $c_p = \frac{\partial H}{\partial T}|_p$ at constant pressure and resolution 128^3 the solid line corresponds to a fit (see eq.(60)). d) Temperature dependence of the energies e_{kin}^c , e_{kin}^i , e_{kin} and $e_q + e_{\text{int}}$ at constant density; equipartition of energy between e_{kin} and $e_q + e_{\text{int}}$ is apparent at low temperatures.

Figure 2.b displays the temperatures dependence of the condensate fraction $|A_0|^2/\rho$ for the four SGLE runs. Observe that the condensation transition previously obtained (in the constant density case) by microcanoni-

cal simulations in references^{13,24} is reproduced and also present (at different critical temperatures) in the constant pressure and chemical potential scans.

The SGLE algorithm directly provides the temperature. It thus allows to easily obtain the specific heat from the data. Figure 2.c displays the specific heat at constant pressure $c_p = \frac{\partial H}{\partial T}|_p$ for the scan at resolution 128^3 . As the ($w = 0$) statistic weight of distribution (21,22) corresponds to that of (standard two-component) second order phase transitions^{28,29}, we thus expect the condensation transition visible on Fig.2.c to be in this standard class. This point is confirmed by the solid lines in Figure 2.c that correspond to a fit with the theoretical prediction given by the renormalization group (RG)

$$c_p = \frac{A^\pm}{\alpha} |\tau|^{-\alpha} (1 + a_c^\pm |\tau|^\Delta + b_c^\pm |\tau|^{2\Delta} + \dots) + B^\pm \quad (60)$$

where $\tau = \frac{T - T_\lambda}{T_\lambda}$ and the $+$ and $-$ signs refer to $T > T_\lambda$ and $T < T_\lambda$, see reference³⁷. The fit was obtained in the following way: first the identification of the transition temperature T_λ is done by finding the zero of the linear interpolation of the second order difference of H , discarding the three closest point to the zero of $|A_0|^2/\rho$. Then, using the critical exponents $\alpha = -0.01126$ and $\Delta = 0.529$ given by the RG the data is fitted as in reference³⁷ over the non-universal constant. The values obtained give $A^+/A^- = 1.42$, to be compared with 1.05 in reference³⁷. This discrepancy is probably due to finite size effects.

Finally on Fig.2.d the temperature dependence at constant density of the different energies (8-10) expressed in terms of hydrodynamical variables is displayed. Observe that the incompressible kinetic energy E_{kin}^i vanishes for low temperatures $T \ll T_\lambda^\rho$, where $T_\lambda^\rho = 3.31$ is the transition temperature at constant density. This is due the disappearance of vortices, that it is also manifest in the density histograms in Fig.1. At low temperature equipartition of energy between the total kinetic energy e_{kin} and quantum plus internal energy $e_q + e_{\text{int}}$, as discussed at the end of section III B, is apparent on the figure.

IV. ENERGY CASCADE, PARTIAL THERMALIZATION AND VORTEX ANNIHILATION

A new mechanism of thermalization through a direct cascade of energy is studied in section IV A. Using initial conditions with mass and energy distributed at large scales, a long transient with partial thermalization of the density waves is obtained at small-scales. Vortex annihilation is observed to take place and is related to mutual friction effects. A bottleneck effect that produces spontaneous self truncation with partial thermalization and a time-evolving effective truncation wavenumber is characterized in section IV B for large dispersive effects at the maximum wavenumber of the simulation.

A. Partial thermalization

We now study the (partial) thermalization of the superfluid Taylor-Green (TG) vortex. This flow, that was first introduced in reference⁶, develops from an initial condition that is prepared by a minimization procedure using the advected real Ginzburg-Landau equation (ARGLE)⁶. The nodal lines of the initial condition ψ_{TG} are the vortex lines of the standard TG vortex and obeys all its symmetries. Numerical integrations are performed with a symmetric pseudo-spectral code, making use of the TG symmetries to speed up the computations and optimize memory use, as described in reference⁶. We use the equivalent to 256^3 and 512^3 collocation points and the coherence length is respectively set to $\xi = \sqrt{2}/80$ and $\xi = \sqrt{2}/160$ giving, in both cases, $\xi k_{\text{max}} = 1.48$.

Vortices and density fluctuations are visualized on Fig. 3. The short time behavior, see Fig. 3.a-c, corresponds to the GPE superfluid turbulent regime previously studied in ref.⁵. A new TGPE thermalization regime where vortices first reconnect into simpler structures and then decrease in size with the emergence of a thermal cloud is present at latter times, see Fig. 3.d-e.

To further study this new TGPE regime, the temporal evolution of e_{kin} , e_{kin}^i , e_{kin}^c , $e_q + e_{\text{int}}$ is displayed in Fig.4.a and the corresponding energy spectra in Fig.4.c. Observe that, at $t = 0$, e_{kin}^i contains almost all the energy because of the highly vortical initial condition. The early times ($t \leq 15$) correspond to the PDE regime of the GPE (1) that was previously reported in references^{5,6}. An energy transfer from e_{kin}^i to density waves is observed.

Continuing the temporal integration the spectral convergence of the GP partial differential equation is lost. The dynamics becomes influenced by the truncation wavenumbers k_{max} and thermalization starts to take place. Two new regimes are observed. The first one for $20 \lesssim t \lesssim 80$ corresponds to a partial thermalization at small-scales is apparent on Fig.4.d-f. Note that equipartition of e_{kin}^c and $e_q + e_{\text{int}}$ starts to establish. This thermalized zone progressively extends to larger wave-numbers. During this phase e_{kin}^i decrease at almost constant rate. It is apparent on Fig.4.b that this phase is delayed by increasing the resolution (at constant ξk_{max}).

Around $t = 80$ (Fig.4.a and f) equipartition is established for each wave-number and e_{kin}^i almost vanishes. The vortices thus disappear, first reconnecting into simpler structures and then decreasing in size (as can be directly observed on density visualizations, pictures not shown). Note that the annihilation of the vortices can be related to the contraction of vortex rings due to mutual friction reported in ref.²⁷. For $t > 80$ the system finally reaches the thermodynamic equilibrium. The absence of vortices and the equipartition of energy between e_{kin}^c and $e_q + e_{\text{int}}$ is a consequence of the low energy initial condition ψ_{TG} as it is apparent in the temperature scan in Fig.2.d. We have thus presented for the first time a new mechanism of thermalization through a direct cascade of energy of the TGPE similar to that of the incompressible

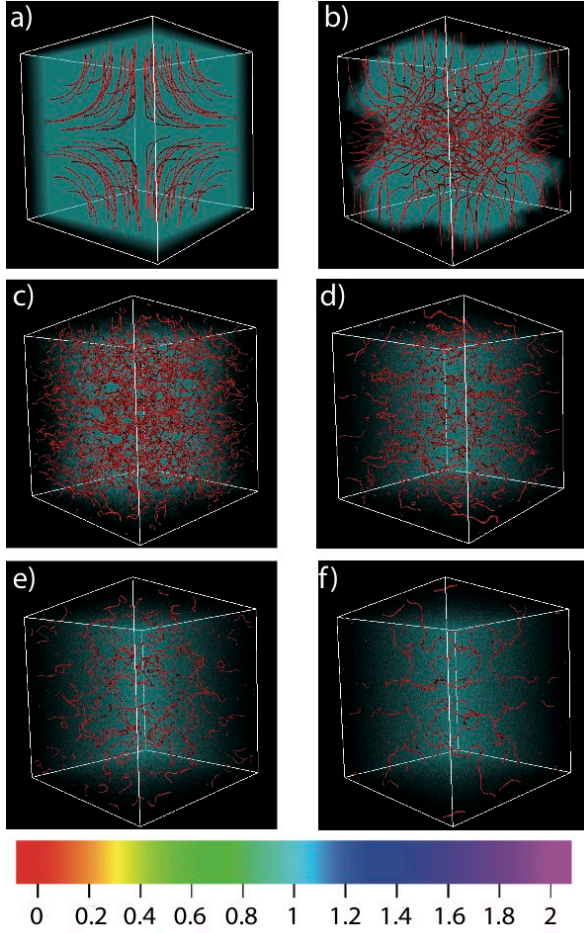


FIG. 3: 3D visualization of density at $t = 0, 5, 10, 20, 31$ and 55 at resolution 512^3 . Vortices are displayed as red isosurfaces and clouds correspond to density fluctuations.

truncated Euler equation reported in reference¹⁸.

B. Dispersive slowdown of thermalization and bottleneck

We now turn to the study of dispersion effects on the thermalization of the TGPE dynamics and on vortex annihilation. To wit, we prepare three different initial conditions with different values of ξk_{\max} using the TG initial condition described in the preceding section. We fix the value of the coherence length to $\xi = \sqrt{2}/20$ and use resolutions of 64^3 , 128^3 and 256^3 corresponding to $\xi k_{\max} = 1.48, 2.97$ and 6.01 respectively. The three initial condition therefore represent the same field at different resolutions.

The temporal evolutions of e_{kin} , e_{kin}^i , e_{kin}^c and $e_q + e_{\text{int}}$ for the three runs (indexed by the resolution) are displayed on Fig.5.a. They are identical until $t \approx 5$ where the run of resolution 64^3 starts to lose its spectral convergence. At $t \approx 20$ all runs appear to have ther-

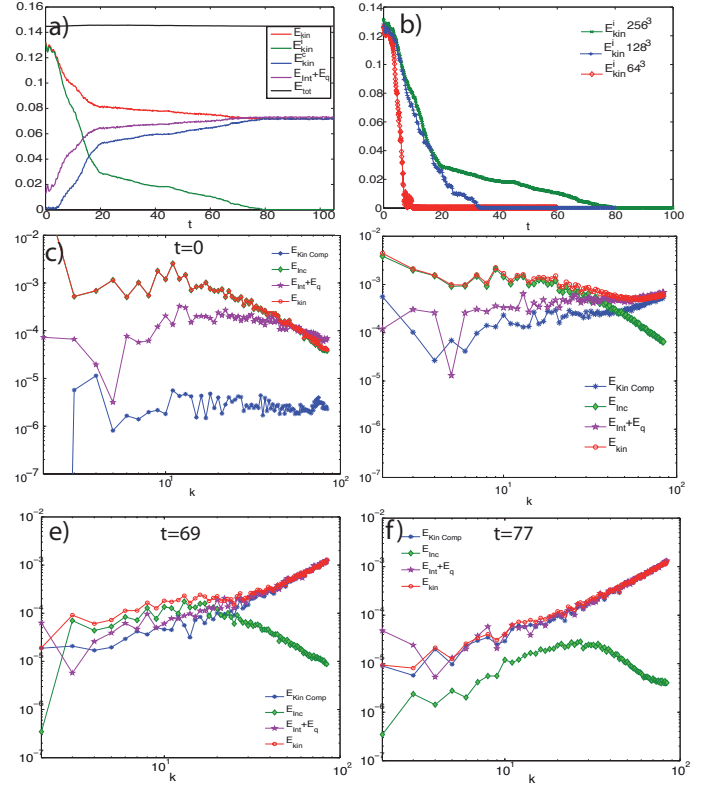


FIG. 4: a) Temporal evolution of energies e_{kin}^c , e_{kin}^i , e_{kin} and $e_q + e_{\text{int}}$. At large times, the incompressible energy vanishes and equipartition of energy between e_{kin} and $e_q + e_{\text{int}}$ is observed. b) Temporal evolution of e_{kin}^i at resolution of 64^3 , 128^3 and 256^3 with constant $\xi k_{\max} = 1.48$. c-f) Energy spectra at $t = 0, 15, 69, 77$ at resolution 256^3 . Figure e) shows that equipartition is reached for all mode.

malized on Fig.5.a. However the kinetic energy spectra on Fig.5.b shows a clear difference between the runs (the dashed line corresponds to k^2 power-law scaling). The high-wavenumber modes of the 64^3 run are thermalized. For the 128^3 run the high-wavenumbers begin to fall down and, at resolution 256^3 , two zone are clearly distinguished. An intermediate thermalized range with an approximative k^2 power-law scaling is followed by a steep decay zone well before $k_{\max} = 85$. Remark that in the 256^3 run the spectral convergence is still ensured and the (partial) thermalization is thus obtained within the GP PDE-dynamics.

The temporal evolution of $e_{\text{kin}}(k)$ for the 256^3 run is displayed in Fig.5.c. The large wave-number k^{-3} power-law behavior at $t = 0$ is an artifact of the high- k decomposition of energies in the presence of vortices (see pp. 2649-2650 of ref.⁶ and³⁸) and a faster decay is recovered as soon as the vortices disappear. The thermalized intermediate zone is observed to slowly extends to smaller wave-numbers. This naturally defines a *self-truncation* wave-number $k_c(t)$ where the energy spectrum starts to

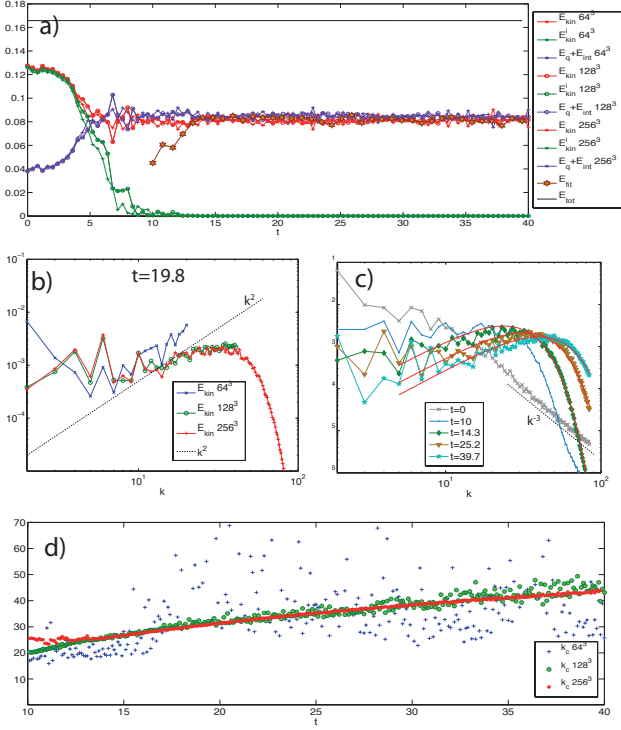


FIG. 5: a) Temporal evolution of energies (as in Fig4.a) for $\xi k_{\text{max}} = 1.48, 2.97$ and 6.01 (resolution $64^3, 128^3$ and 256^3 respectively). Yellow stars are the kinetic energy reconstructed from fit data using eq.(62). b) Kinetic energy spectrum at $t = 17.4$ for $\xi k_{\text{max}} = 1.48, 2.97$ and 6.01 ; the dashed black line indicates k^2 power-law scaling. c) Temporal evolution of kinetic energy spectrum; the solid red lines correspond to fits using eq.(61) and the dashes black line indicate k^{-3} power-law scaling. d) Temporal evolution of effective self-truncation wavenumber k_c (Eq.(61)) at different resolutions.

drastically decrease.

In order to determine $k_c(t)$ we have tested fits to $e_{\text{kin}}(k)$ using two type of trial spectra with three free parameters: $e_{\text{fit I}}(k) = A(t)k^{-n} \exp[-2\delta(t)k]$ and $e_{\text{fit II}}(k) = A(t)k^{-n} \exp[-\gamma(t)k^2]$. The $e_{\text{fit II}}(k)$ fit was found to work better in the sense that it both gives the correct $n = -2$ prefactor at intermediate and large times and also gives a better fit to the data at high k (data not shown). Fixing the prefactor at the value $n = -2$, we finally define our working two-parameter fit as:

$$e_{\text{fit}}(k, t) = A(t)k^2 e^{-\left[\left(\frac{9\pi}{16}\right)^{\frac{1}{3}} \left(\frac{k}{k_c(t)}\right)^2\right]} \quad (61)$$

$$e_{\text{fit}}(t) = \int_0^{k_{\text{max}}} e_{\text{fit}}(k, t) dk. \quad (62)$$

The factor $(9\pi/16)^{1/3}$ in eq.(61) was set in order to obtain the limits $Ak_c^3/3$ and $Ak_{\text{max}}^3/3$ for $e_{\text{fit}}(t)$ when $k_{\text{max}} \rightarrow \infty$ and $k_c \rightarrow \infty$ respectively. The fits are also displayed in Fig.5.c. They are in good agreement with the data after vortices have disappeared. The temporal evolution of

$e_{\text{fit}}(t)$ is displayed in Fig.5.a. It does converge to the thermalized value of the energy. Finally the temporal evolution of the self-truncation wavenumber $k_c(t)$, which seems to have a well defined limit at infinite resolution, is displayed in Fig.5.d for the three runs.

An open question is whether k_c is bounded in time in the PDE regime where $k_c \ll k_{\text{max}}$. In other words, is thermalization of the $\xi k_{\text{max}} \gg 1$ truncated system simply delayed or completely inhibited when ξk_{max} is large enough? Note that this problem is related to the classical Fermi-Pasta-Ulam-Tsingu problem³⁹.

To try to answer this question within the Taylor-Green framework would be computationally very expensive as long runs should be performed at arbitrarily high resolutions.

A simple alternative idea to study this problem is to use initial data for the TGPE generated by the SGLE with a variable truncation wavenumber k_c^{in} , set to a target value of k_c , smaller than the maximum truncation wavenumber k_{max} allowed by the resolution. This SLGE-generated initial data can then be used to run the TGPE at a given value of ξk_c with arbitrarily large values of ξk_{max} . A number of runs were performed at resolution 64^3 with various values of k_c^{in} , ξ , and initial energy e^{in} (see legend on Fig.6). The result of these computations are compared with the above Taylor-Green runs (see Fig.5) and displayed on Fig.6. Because of the steep decay of the energy spectrum for $k \gg k_c$, the self-truncation wavenumber is determined using the integral formula

$$k_c = \sqrt{\frac{5}{3} \frac{\int_0^{k_{\text{max}}} k^2 e_{\text{kin}}(k) dk}{\int_0^{k_{\text{max}}} e_{\text{kin}}(k) dk}}. \quad (63)$$

A general growth in time of k_c is apparent on Fig.6.a for both the Taylor-Green runs and the SGLE-generated initial data, showing similar behavior. In order to check for self-similar regime a parametric Log-Log representation dk_c/dt v.s. k_c has been used on Fig.6.b and Fig.6.c. With this representation, a self-similar evolution $k_c(t) \sim t^\alpha$ corresponds to a line of slope $\beta = (\alpha - 1)/\alpha$. Figure 6.b, shows transient self-similar evolutions, that all terminate by a vertical asymptote, corresponding to logarithmic growth ($\alpha = 0$). This self-truncation takes place for small values of k_c/k_{max} strongly suggesting that the self-truncation happens in a regime independent of cut-off. Finally, Fig.6.c suggests that, depending on initial conditions, self-truncation can take place at arbitrarily values of ξk_c .

As the dynamics of modes at wave-numbers larger than k_c is weakly nonlinear, it should be amenable to a description in terms of wave turbulence theory; this could perhaps explain the slowdown of the thermalization in this zone. The new regime indicates that total thermalization is delayed when increasing the amount of dispersion (controlled by ξk_{max}) but is preceded by a partial thermalization (quasi-equilibrium up to k_c) within a PDE.

We now turn to estimations of order of magnitude relevant to physical BEC. At low-temperature, the GPE is

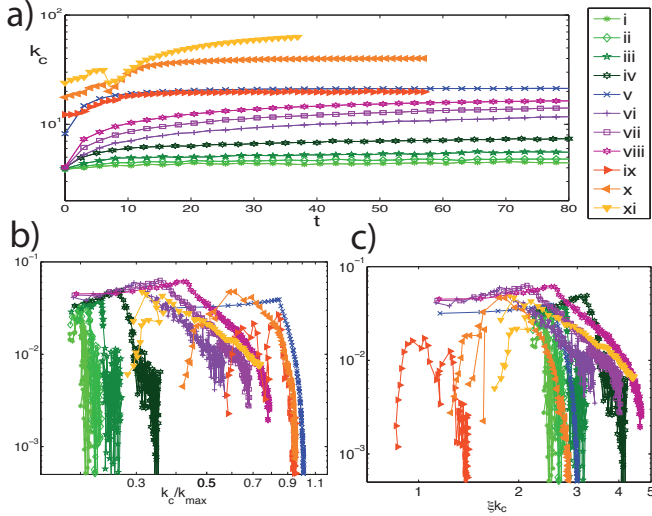


FIG. 6: a) Evolution of the self-truncation wavenumber k_c . Curves i-iv: $\xi = 2\sqrt{2}/5$, $k_c^{\text{in}} = 4$, $E^{\text{in}} = 0.1, 0.2, 0.4, 1$; v: $\xi = \sqrt{2}/10$, $k_c^{\text{in}} = 8$, $E^{\text{in}} = 0.2$; vi-viii: $\xi = \sqrt{2}/5$, $E^{\text{in}} = 0.1, 0.2, 0.4$ (i-viii in resolution 64^3); ix-xi: Taylor-Green resolutions 64^3 , 128^3 and 256^3 . b-c) Parametric representation dk_c/dt v.s. k_c/k_{\max} and dk_c/dt v.s. ξk_c (same labels as in fig. a).

known³ to give an accurate description of the (classical) dynamics of physical BEC at scales larger than the interatomic separation ℓ . At finite temperature the TGPE gives a good approximation of Bose-Einstein condensate (BEC) only for the phonon modes with high occupation number, see^{3,13}. At very low temperature thus only a limited range of low-wavenumber density waves are in equipartition.

This limited range has consequences on the low-temperature thermodynamics of BEC that can be obtained by the following considerations. The equipartition range is determined by the relation $k \leq k_{\text{eq}}$ with $\hbar\omega_B(k_{\text{eq}}) = k_B T$ where the Bogoliubov dispersion relation $\omega_B(k)$ is given by

$$\omega_B(k) = k \sqrt{\frac{g|A_0|^2}{m} + \frac{\hbar^2}{4m} k^2}. \quad (64)$$

The coherence length ξ defined in eq. (7) can be expressed in terms of the s -wave scattering length \tilde{a} defined by $g = 4\pi\tilde{a}\hbar^2/m$ and the mean inter-atomic particle distance $\ell \equiv n^{-1/3} \approx |A_0|^{-2/3}$ as

$$\xi = (8\pi n \tilde{a})^{-1/2} = \ell \frac{1}{\sqrt{8\pi}} \left(\frac{\ell}{\tilde{a}} \right)^{1/2}. \quad (65)$$

For weakly interacting BEC the coherence length thus satisfies $\xi \gg \ell$. The equipartition wavenumber k_{eq} explicitly reads

$$k_{\text{eq}} = \left[\frac{\sqrt{32k_B^2 m^2 T^2 \xi^4 + \hbar^4}}{4\xi^2 \hbar^2} - \frac{1}{4\xi^2} \right]^{1/2}. \quad (66)$$

Using the Bose-Einstein condensation temperature of non-interacting particles (valid for $\tilde{a} \ll \ell$)³

$$T_\lambda = \frac{2\pi\hbar^2}{k_B m} \left[\frac{n}{\zeta(3/2)} \right]^{2/3} \quad (67)$$

where $\zeta(3/2) = 2.6124\dots$, the equipartition wavenumber k_{eq} can be expressed as

$$k_{\text{eq}} = \frac{1}{2\xi} \left[\sqrt{1 + \frac{128\pi^2}{\zeta(3/2)^{4/3}} \frac{\xi^4}{\ell^4} \frac{T^2}{T_\lambda^2}} - 1 \right]^{1/2} \quad (68)$$

Observe that k_{eq} varies from $k_{\text{eq}} = 0$ at $T = 0$ to wavenumber of order $k_{\text{eq}} \sim \ell^{-1}$ at T_λ and it is equal to $k_\xi = 2\pi/\xi$ at T^* defined by

$$T^* = 4\pi\sqrt{1 + 8\pi^2\zeta(3/2)^{2/3}} \frac{\tilde{a}}{\ell} T_\lambda. \quad (69)$$

Thus the thermodynamic of physical BEC at low-temperature (e.g. specific heat scaling as T^3) can be recovered from the TGPE thermodynamics by setting $k_{\max} = k_{\text{eq}}(T)$.

In experimental turbulent weakly interacting BEC such as⁴⁰ the value of ξk_{eq} is large because $T^*/T_\lambda \sim \frac{\tilde{a}}{\ell} \ll 1$ and therefore the corresponding TGPE should have a large ξk_{\max} . Thus the thermalization slowdown caused by the dispersive bottleneck should be in principle present in physical BEC, unless it is overwhelmed by other relaxation mechanisms⁴¹.

V. METASTABILITY OF COUNTERFLOW, MUTUAL FRICTION AND KELVIN WAVES

Counter-flow states with non-zero values of momentum generated by the new SGLE algorithm and their interaction with vortices are investigated in this section. The counter-flow states are shown to be metastable under SGLE evolution; the spontaneous nucleation of vortex ring and the corresponding Arrhenius law are characterized in section VA. Dynamical counter-flow effects are investigated in section VB using vortex rings and vortex lines patterns that are exact solutions of the GPE. Longitudinal and transverse mutual friction effects are produced and measured. An anomalous translational velocity of vortex ring is exhibited and is quantitatively related to the effect of thermally excited finite-amplitude Kelvin waves. Orders of magnitude are estimated for the corresponding effects in BEC and superfluid ^4He .

A. Metastability of grand canonical states with counterflow

1. Thermodynamic limit of states with nonzero counterflow

The counterflow states with $\mathbf{W} \neq \mathbf{0}$ are determined by thermal fluctuations around the minima of the energy F

eq.(22). These minima correspond to the solution of

$$\frac{\delta F}{\delta \psi^*} = 0 = -\frac{\hbar^2}{2m} \nabla^2 \psi + g \mathcal{P}_G[|\psi|^2] \psi - \mu \psi + i \hbar \mathbf{W} \cdot \nabla \psi \quad (70)$$

that are plane-waves of the form

$$\psi(x; \mathbf{v}_s) = g^{-\frac{1}{2}} \sqrt{\mu - m \mathbf{W} \cdot \mathbf{v}_s + \frac{m v_s^2}{2}} e^{-i \frac{m}{\hbar} \mathbf{v}_s \cdot \mathbf{x}}, \quad (71)$$

where the velocity \mathbf{v}_s indexes the different solutions.

In the thermodynamic limit, the Galilean group defined by the transformations (11-14) is continuously indexed by the velocity \mathbf{v}_G . All wavefunctions (71) are thus equivalent by Galilean transformation (and redefinition of the chemical potential). Under the Galilean transformation (11) the energy F is transformed as $F' = F - (m \mathbf{W} \cdot \mathbf{v}_G - m v_G^2/2)N + \mathbf{v}_G \cdot \mathbf{P}$. Note that, among all the minima of F the one with $\mathbf{v}_s = \mathbf{W}$ minimizes F' . This state corresponds to a condensate moving with uniform velocity \mathbf{W} . The $\mathbf{W} \cdot \mathbf{P}$ term is thus only imposing a Galilean transformation of the global minimum.

However, when working in a finite volume, the Galilean transformation is quantized (see eq. (18)) and the minima of F' of lowest energy corresponds to a condensate moving with the uniform velocity \mathbf{v}_s closest to \mathbf{W} . At finite temperature and volume, when \mathbf{W} is not too large, we thus have two ways to produce momentum in the system. The first one corresponds to Galilean transformations and the second one to fluctuations of the exited phonons; with the momentum of phonons imposed by the term $\mathbf{W} \cdot \mathbf{P}$ in the grand canonical distribution (21), and $\mathbf{v}_s = 0$ in (71). Metastability is thus expected when $\mathbf{W} \neq 0$ with quasi-equilibrium corresponding to condensates at different wavenumbers with an energy barrier between each of those states.

In the context of the Landau two-fluid model¹ the velocity \mathbf{v}_s of the condensate corresponds to the superfluid velocity and the momentum carried by the exited phonons is written as $\mathbf{P} = \rho_n(\mathbf{v}_n - \mathbf{v}_s)$ where ρ_n and \mathbf{v}_n are called the normal density and velocity respectively. The counterflow velocity defined by $\widehat{\mathbf{W}} = \mathbf{v}_n - \mathbf{v}_s$ is a Galilean invariant.

The above discussion shows that, in general the variable \mathbf{W} in the SGLE (41) corresponds to $\mathbf{W} = \mathbf{v}_n$. In the thermodynamic (infinite volume) limit $\mathbf{W} = \mathbf{v}_s$ and there is thus no counterflow $\widehat{\mathbf{W}} = \mathbf{v}_n - \mathbf{v}_s = \mathbf{0}$. For finite-size systems, in general $\mathbf{v}_s \neq \mathbf{W}$ and $\widehat{\mathbf{W}} \neq \mathbf{0}$.

We thus define (when $v_s = 0$) the normal density by

$$\rho_n = \left. \frac{\partial P_z}{\partial w_z} \right|_{w_z=0}. \quad (72)$$

2. Thermodynamics of metastable states at small temperature and small counterflow

To validate the SGLE in the presence of counterflow two scans are performed at constant density using a resolution of 64^3 and $\xi k_{\max} = 1.48$. The condensate is set

at $\mathbf{k} = 0$ in the SGLE initial data and the temperature is fixed to $T = 0.2$. This low temperature allows us to increase the value of the counterflow w_z (hereafter we set $w_x = w_y = 0$) keeping the condensate at $\mathbf{k} = 0$. The dependence of the momentum P_z on w_z is presented in Fig.7.a. The solid line corresponds to

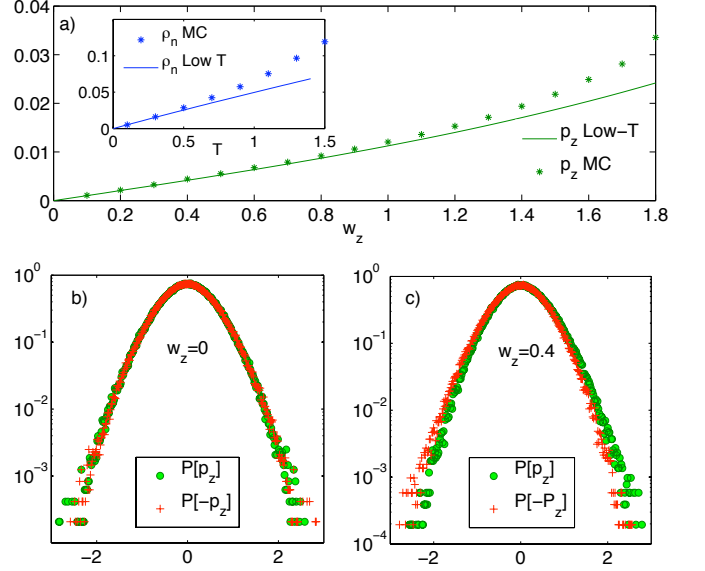


FIG. 7: Counterflow dependence of momentum P_z ($w_x = w_y = 0$). Inset: Temperature dependence of $\rho_n = \left. \frac{\partial P_z}{\partial w_z} \right|_{w_z=0}$. b) Histograms of momentum P_z and $-P_z$ (in log - lin) with no counterflow at $T = 1$. No asymmetry is observed. c) Histograms of momentum P_z and $-P_z$ with counterflow $w_z = .4$ at $T = 1$. An asymmetry, induced by counterflow, is apparent. Observe that both histograms are centered at $P_z = 0$.

the low-temperature calculations (eq. (58) and appendix B eqs.(B9)). The second run correspond to a temperature scan (at low counterflow $w_z = .1$). The temperature dependence of ρ_n is displayed together with the low-temperature calculation on the inset of Fig.7.a.

Figure 7.a-b display histograms of P_z and $-P_z$ in physical space, both obtained at $T = 1$ with the condensate at $\mathbf{k} = 0$ but with zero and non-zero counterflow. Observe that the histograms are both centered at $P_z = 0$ but the non-zero counterflow induces an asymmetry in the statistical distribution that yields a non-zero value for the mean momentum.

3. Spontaneous nucleation of vortex rings and Arrhenius law

At temperatures and counterflow velocities large enough the stochastic process defined by the SGLE can jump between different metastable states. In this section, we show how the different states are explored, un-

der SGLE evolution, by spontaneous nucleation of vortex rings. To wit, we present a numerical integration of SGLE at resolution 64^3 with $\xi k_{\max} = 1.48$. With this choice of parameters the velocity quantum (18) is fixed to 0.2. The temperature is set to $T = 0.775$ and the counterflow to $w_z = 0.8$. The condensate is set at $\mathbf{k} = \mathbf{0}$ in the SGLE initial data and the density is kept constant to $\rho = 1$.

The temporal evolution of the momentum P_z is displayed in Fig.8.a (right scale). Observe that the system

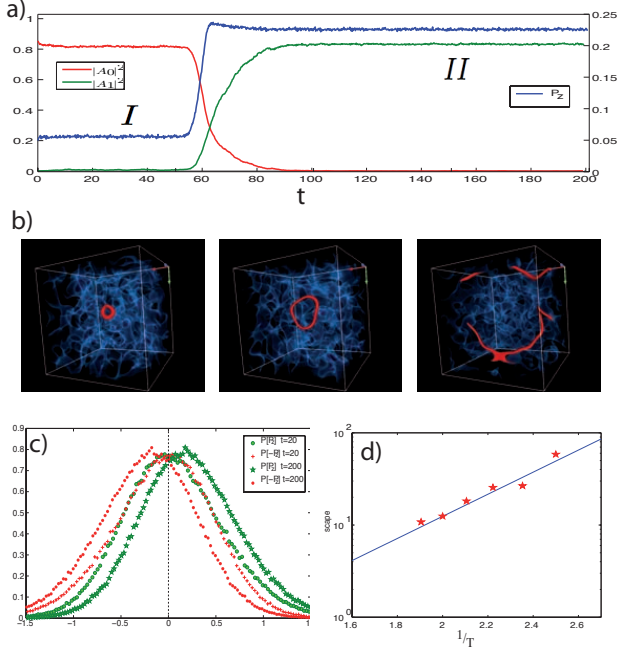


FIG. 8: a) Temporal evolution of $|A_0|^2$ and $|A_1|^2$ (left scale) under SGL dynamics. Observe that there are two *quasi*-stationary states (*I* and *II*) and the condensate makes a transition from $k = 0$ to $k = 1$. The temporal evolution of the momentum p_z is displayed in the same plot (right scale). Observe that transition from one state to the other is accompanied by an increase of momentum. b) 3d visualization of density at $t = 54.5$, $t = 56$ and $t = 60.5$; the blue clouds corresponds to density fluctuations and the vortices are displayed as red isosurface (see colorbar on Fig.10 below). c) Histogram of momentum p_z and $-p_z$ at the two *quasi*-stationary states (*I* and *II*) in *lin-lin* plot. d) Arrhenius law: data from SGL dynamics (points) and theoretical eq. (73) (solid line).

first spends some time at the state (*I*) with $P_z \approx 0.05$ and that, around $t = 55$, it jumps to the state (*II*) with $P_z \approx 0.225$. These two metastable states correspond to quasi-equilibrium at $\mathbf{k} = \mathbf{0}$ and $\mathbf{k} = \mathbf{1}$ as is apparent in Fig.8.a (left scale) where the temporal evolution of $|A_0|^2$ and $|A_1|^2$ (see eq. (15)) are displayed.

To illustrate the dynamic of the condensate jump from $\mathbf{k} = \mathbf{0}$ to $\mathbf{k} = \mathbf{1}$ 3d visualization of the density at $t = 54.5$, $t = 56$ and $t = 60.5$ are presented on Fig.8.b. The wavefunction ψ is first low-pass filtered and the density is then

visualized using the VAPOR⁶⁴ software. At early times ($t < 50$, pictures not shown) there were no vortices in the box. At $t \approx 54$ a vortex ring is nucleated, then it increases its size under SGLE evolution until it reconnects with the neighbor rings (recall that periodic boundary condition are used). The ring finally contracts and disappears (pictures not shown). During this evolution, the local phase defect of the ring becomes global and changes the condensate wavenumber. Histograms of momentum P_z and $-P_z$ in the two metastable states *I* and *II* are presented in Fig.8.c in a *lin-lin* plot. Observe that both metastable states are asymmetrical as in Fig.7.c. However, *I* is centered at $P_z = 0$ and *II* at $P_z = 0.2$, respectively corresponding to the wavenumbers $\mathbf{k} = \mathbf{0}$ and $\mathbf{k} = \mathbf{1}$.

It is well known that the the escape time of a metastable quasiequilibrium is given, in general, by an Arrhenius law^{42,43}

$$t_{\text{esc}} \sim t_c e^{-\beta \Delta F}, \quad (73)$$

where ΔF is the activation energy of the nucleation solution and t_c is a characteristic time. Here, the nucleation solution is given by a vortex ring that satisfies $\frac{\partial F}{\partial \psi^*} = 0$. The energy barrier is thus determined by $\Delta F = H_{\text{ring}}(R^*) - \mathbf{V}_{\text{ring}} \cdot \mathbf{P}_{\text{ring}}(R^*)$, where the analytic expressions for the energy H_{ring} , the momentum \mathbf{P}_{ring} and the radius are given by

$$V_{\text{ring}} = \frac{\hbar}{2m} \frac{1}{R^*} \left[\ln \left(\frac{8R^*}{\xi} \right) - a \right] \quad (74)$$

$$P_{\text{ring}}^* = \frac{2\pi^2 \hbar \rho_{\infty}}{m} R^{*2} \quad (75)$$

$$H_{\text{ring}}^* = \frac{2\pi^2 \hbar^2}{m^2} \rho_{\infty} R^* \left[\ln \left(\frac{8R^*}{\xi} \right) - 1 - a \right] \quad (76)$$

where ρ_{∞} is the density at the infinity and a is a core model-depending constant with value $a = 0.615$ for the GPE vortices⁴. Formulae (74-76) and the value of a have been numerically validated in reference⁴⁴ using a Newton method⁴⁵⁻⁴⁷.

In order to numerically check that the escape time indeed follows an Arrhenius law we now perform runs with $\xi k_{\max} = 1.48$ and resolution 32^3 . The counter-flow is fixed at $w = 1.4$ and the condensate is set initially at $\mathbf{k} = \mathbf{0}$ (constant density $\rho = 1$). At each fixed temperature T , several numerical integration of SGLE are performed and the escape times for the condensate to leave the wavenumber $\mathbf{k} = \mathbf{0}$ are measured. These escape times are then averaged over more than 10 realizations. Figure 8.d displays the escape time t_{esc} obtained in this way as a function of the inverse temperature $1/T$ in *log-lin*. The slope of the solid line is computed using the analytic formulae (74-76) of ΔF . Both, numerical and theoretical Arrhenius laws are in good agreement. It is thus possible to use the SGLE dynamics to prepare metastable states with finite value of counterflow and lifetime quantitatively given by the Arrhenius law (73).

B. Dynamical effects of finite temperature and counterflow on vortices

We now turn to the study the dynamical effects of counterflow on TGPE vortex evolution, we set up finite temperature and finite counterflow initial states that also contain vortices. Two cases are investigated: (i) vortex lines, in a crystal-like pattern that does not produce self induced velocity and (ii) vortex rings, producing self induced velocity.

1. Lattice of vortex lines

To numerically study the effect of counterflow on vortices we prepare an initial condition ψ_{lattice} consisting in a periodical array (of alternate sign) straight vortices similar to those used in ref.⁴⁸ to study the scattering of first sound. The lattice (obtained with a Newton method^{45–47}) is stationary exact solution of GPE. As the vortices are separated by a distance $d = \pi$, they can be considered isolated in the limit $\xi \ll d$. Note that this limit is obtained when the resolution is increased at constant ξk_{max} . To include temperature effect we prepare absolute equilibria ψ_{eq} using SGLE with the counterflow aligned with the z -axis (perpendicular to the vortices in ψ_{lattice}). Then the initial condition $\psi = \psi_{\text{lattice}} \times \psi_{\text{eq}}$ is evolved with the TGPE. Several runs were performed at different resolutions (with $\xi k_{\text{max}} = 1.48$), temperature and counterflow values (see legend on Fig. 9.b).

Figure 9.a displays the temporal evolution of $(R_{\parallel}, R_{\perp})$ the respectively parallel and perpendicular component of the vortex filament to the counterflow for $T = 0.5, 1$ and $w_z = 0.4$. The trajectories are obtained by first averaging along the direction of the vortices, then the (averaged) coordinate of the vortices is found by seeking the zero of the reduced $2d$ wavefunction. Observe that the vortex, originally located at $(\frac{3\pi}{4}, \frac{3\pi}{4})$, moves in the direction of the counterflow and its velocity clearly depends on the temperature. It is apparent that a perpendicular movement is also induced at short times. This movement has two phases, the first one is related to an adaptation and makes the crystal-like lattice slightly imperfect. Then the perpendicular movement almost stops (a very small slope can be observed for long time integration). The initial phase where the parallel and perpendicular motions have similar velocities lasts longer when ξ/d is decreased by increasing the resolution (data not shown). Observe that the imperfection of the lattice in the final configurations is almost equal for the two temperatures presented in Fig.9.a, but the parallel velocities are considerably different. Thus, the self-induced parallel velocity caused by the slight imperfection of the lattice is very small and is not driving the longitudinal motion.

We now concentrate on the measurement of R_{\parallel} for which the present configuration is best suited.

R_{\parallel} has a linear behavior, that allows to directly measure the parallel velocity v_{\parallel} . The temperature depen-

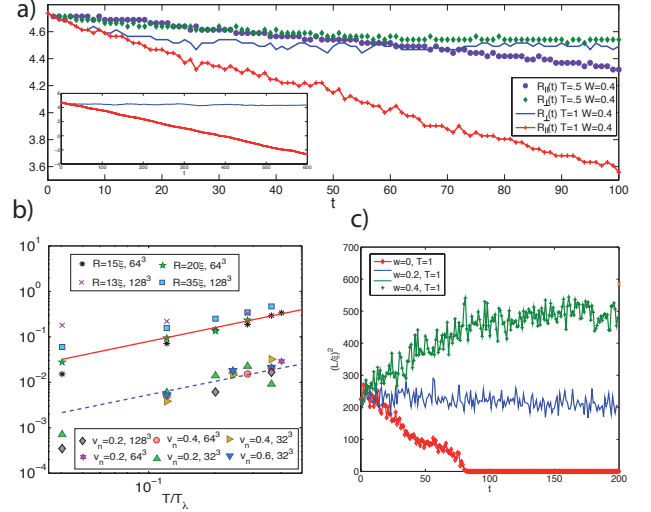


FIG. 9: a) Trajectory of a straight vortex in the crystal pattern for $T = 1$, $T = 0.5$ and $w_z = .4$, at resolution 64^3 . Inset: run with $T = 1$ until $t = 600$. b) Temperature dependence ($T_\lambda = 3.31$) of the advection velocity v_{\parallel}/w_z for the lattice and $\Delta v_L/u_i$ for the vortex rings (resolutions 32^3 - 128^3). The dashed line corresponds to eq.(78) with $B' = 0.83$ and the solid line to the theoretical prediction (89). c) Temporal evolution of the square of the length of the vortex ring for different values of counterflow, $T = 1$ and initial radius $R = 15\xi$ at resolution 64^3 .

dence of v_{\parallel}/w_z is presented on Fig.9.b for different values of w_z and d/ξ (corresponding to the different resolutions).

For superfluid vortices the standard phenomenological dynamic equation of the vortex line velocity v_L is⁴

$$\mathbf{v}_L = \mathbf{v}_{sl} + \alpha \mathbf{s}' \times (\mathbf{v}_n - \mathbf{v}_{sl}) - \alpha' \mathbf{s}' \times [\mathbf{s}' \times (\mathbf{v}_n - \mathbf{v}_{sl})], \quad (77)$$

where \mathbf{s}' is the tangent of the vortex line, \mathbf{v}_{sl} is the local superfluid velocity that is the sum of the ambient superfluid velocity \mathbf{v}_s and the self-induced vortex velocity \mathbf{u}_i and $\mathbf{v}_n = \mathbf{w} + \mathbf{v}_s$ is the normal velocity. The constants α, α' depend on the temperature. The existence of the transverse force (related to the third term of r.h.s. in Eq.77) has been subject of a large debate in the low-temperature community in the last part of the 90's^{49–55} and the controversy is still not resolved. Applied to the present case, eq.(77) predicts $v_{\perp} = -\alpha w_z$ and $v_{\parallel} = \alpha' w_z$. The value of the constant α' , related to the transverse force, depends on the normal density and the scattering section. It can be expressed as

$$\alpha' = B' \frac{\rho_n}{2\rho} \quad (78)$$

where B' is a order one constant⁴. A fit to the measured values of v_{\parallel}/w_z yields $B' = 0.8334$, see fig.9.b. We thus conclude that finite-temperature TGPE counterflow effects measured on R_{\parallel} for the crystal pattern are in quantitative agreement with standard phenomenology

(eq.(77)). We have seen above that the effect on R_\perp is of the same order of magnitude that the one on R_\parallel , as long as crystal imperfection does not come into play.

2. Vortex rings

We now turn to study the effect of counterflow on vortex rings. The initial condition is prepared as in the previous section but with the crystal ψ_{lattice} replaced by a vortex ring ψ_{ring} , that is an exact stationary (in a co-moving frame) solution of GPE. The plane containing the vortex rings of radius R is perpendicular to the counterflow and the rings are numerically obtained by a Newton method^{45–47}.

In the case of vortex rings the general formula (77) yields

$$\dot{R} = -\alpha(u_i - w_z) \quad (79)$$

$$v_L = v_s + (1 - \alpha')u_i + \alpha'w_z, \quad (80)$$

where u_i denotes the ring velocity at zero temperature, explicitly given by V_{ring} in formula (74) (replacing R^* by the corresponding radius). In the special simple case $w_z = 0$, a finite-temperature contraction of the vortex ring is predicted. This transverse effect was first obtained and measured by Berloff, using a finite-difference scheme version of the TGPE that exactly conserves the energy and particle number²⁷.

The temporal evolution of the square of the vortex length of a ring of initial radius $R = 15\xi$ at temperature $T = 1$ and counterflow $w_z = 0, 0.2$ and 0.4 is displayed on Fig.9.c. For $w = 0$, the dynamics under TGPE evolution reproduces the Berloff ring contraction²⁷. The temperature dependence of the contraction obtained for $w = 0$ (data not shown) quantitatively agrees with Berloff's results. A dilatation of vortex rings is apparent on Fig.9.c for w larger than the measured vortex ring velocity $v_L = 0.23$.

However, v_L has a very strong dependence on temperature that is also present for $w = 0$. The temperature dependence of $\Delta v_L/u_i$ where $\Delta v_L = u_i - v_L$ and is displayed on Fig.9.b. We have checked that the velocity v_L directly measured at $T = 0$ is indeed given by u_i . Equation (77) predicts (in the absence of counterflow) a longitudinal velocity for the vortex ring $v_L = (1 - \alpha')u_i$. Observe that $\Delta v_L/u_i$ is one order of magnitude above the transverse mutual friction coefficient measured in the perfect crystal.

3. Anomalous translational velocity and Kelvin waves

In this section we relate the finite temperature slowdown to the anomalous translational velocity of vortex ring with finite-amplitude Kelvin waves reported in refs.^{56,57}. Kelvin waves are clearly observed in 3d visualizations of vortex rings driven by TGPE as it is apparent on fig.10 obtained in the same way that fig.8.b.

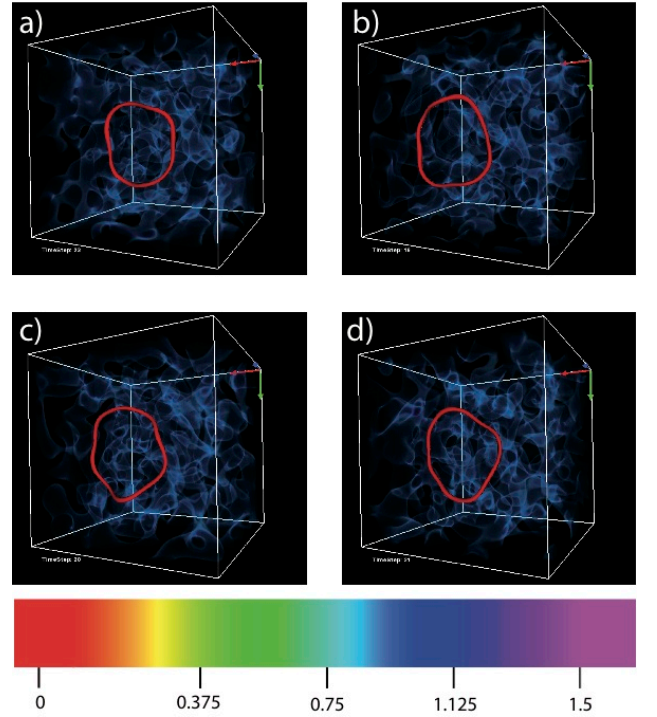


FIG. 10: 3d visualization of density at $t = 18, 19, 20$ and 21 at temperature $T = 1$. Blue cloud correspond to density fluctuations and a vortex ring of radius $R = 20\xi$ with thermally excited Kelvin waves is displayed in red isosurfaces

Following reference⁵⁷, Kelvin waves of amplitude A and wavelength $2\pi R/N$ on a ring of radius R are parametrized, in cylindrical coordinates r, ϕ and z , as

$$x = (R + A \cos N\phi) \cos \phi \quad (81)$$

$$y = (R + A \cos N\phi) \sin \phi \quad (82)$$

$$z = -A \sin \phi. \quad (83)$$

In the limit $N \gg 1$ the dispersion relation $\omega(k)$ of the Kelvin wave (81-83) is given by⁵⁶

$$\omega(k) = \frac{\hbar}{2m} k^2 \left[\ln \left(\frac{8R}{\xi} \right) - a \right] \quad (84)$$

where $k = N/R$ and a is the core model-dependent constant in formula (74).

The anomalous translational velocity caused by an excited Kelvin wave was first reported by Kiknadze and Mamaladze⁵⁶ in the framework of the local induction approximation (LIA). The effect was then obtained and numerically characterized within the Biot-Savart equation by Barenghi et al.⁵⁷. The anomalous translational velocity v_a of a vortex ring reads (in the limit $N \gg 1$, see eq. (26) of reference⁵⁶)

$$v_a \approx u_i \left(1 - \frac{A^2 N^2}{R^2} \right) \quad (85)$$

where $u_i = V_{\text{ring}}$ is the self-induced velocity (74) without Kelvin waves.

The variation of the energy of a vortex ring caused by a (small amplitude) Kelvin wave can be estimated as

$$\Delta E = \frac{dH}{dR} \frac{\Delta L}{2\pi} \quad (86)$$

where H is the energy given by Eq.(76) and the length variation ΔL produced by the Kelvin wave (81-83) is given, at lowest order in the amplitude A/R , by $\Delta L = \pi A^2 N^2 / R$. Assuming equipartition of the energy of Kelvin waves with the heat bath implies $\Delta E = k_B T$, which yields the value of $A^2 N^2 / R^2$ as function of T :

$$\frac{A^2 N^2}{R^2} = \frac{m^2 k_B T}{\pi^2 \rho \hbar^2 R (\log \frac{8R}{\xi} - a)}. \quad (87)$$

The equipartition law (87) can also be directly obtained as the classical limit of the quantum distribution computed by Bareghi *et al.*⁵⁸, up to a redefinition of the core constant model a (see eq.(25) in reference⁵⁸).

We finally assume that the slowing down effect of each individual Kelvin wave is additive and that the waves populate all the possible modes. Kelvin waves are bending oscillations of the quantized vortex lines, with wavenumber $k \lesssim 2\pi/\xi$. The total number of modes can thus be estimated as

$$\mathcal{N}_{\text{Kelvin}} \approx 2\pi R / \xi. \quad (88)$$

Replacing $A^2 N^2 / R^2$ in eq.(85) by eq.(87) and multiplying by the total number of waves $\mathcal{N}_{\text{Kelvin}}$ we obtain the following expression for the anomalous translational effect due to thermally excited Kelvin waves

$$\frac{\Delta v_L}{u_i} \equiv \frac{u_i - v_a}{v_a} \approx \frac{2k_B T m^2}{\pi \rho \xi \hbar^2} \frac{1}{\log \frac{8R}{\xi} - a} \quad (89)$$

The temperature dependence of the equipartition estimate (89) of the thermal slowdown is plotted on Fig.9.b (top straight line). The data obtained from the measurements of the rings velocity in the TGPE runs is in very good agreement with the estimate (89).

As discussed in refs.^{3,13} the TGPE gives a good approximation of Bose-Einstein condensate (BEC) only for the modes with high occupation number. In this spirit quantum effects on the Kelvin waves oscillations must also be taken into account to obtain the total slowing down effect in a BEC. The TGPE estimation (89) can be adapted to weakly interacting BEC by the following considerations.

At very low temperature, only a limited range of low-wavenumber Kelvin waves are in equipartition. This range is determined by the relation $k \leq k_{\text{eq}}$ with $\hbar\omega(k_{\text{eq}}) = k_B T$ and the dispersion relation (84), it reads:

$$k_{\text{eq}} = \sqrt{\frac{k_B T 2m}{\hbar^2 [\ln(\frac{8R}{\xi}) - a]}} \quad (90)$$

and can also be expressed as

$$k_{\text{eq}} = \sqrt{\frac{4\pi n^{2/3}}{\zeta(\frac{3}{2})^{2/3} [\ln(\frac{8R}{\xi}) - a]}} \left(\frac{T}{T_\lambda}\right)^{1/2}. \quad (91)$$

where T_λ is the Bose-Einstein condensation temperature of non-interacting particles (67) and the relation between the interatomic distance ℓ and the vortex-core size ξ are given in Eq.(65).

Observe that k_{eq} varies from $k_{\text{eq}} = 0$ at $T = 0$ to wavenumber of order $k_{\text{eq}} \sim \ell^{-1}$ at T_λ and it is equal to $k_\xi = 2\pi/\xi$ at T^* defined by

$$T^* = 8\pi^2 \zeta(\frac{3}{2})^{2/3} [\ln(\frac{8R}{\xi}) - a] \left(\frac{\tilde{a}}{\ell}\right) T_\lambda. \quad (92)$$

Therefore at temperatures $T^* < T < T_\lambda$ the energy of all Kelvin waves are in equipartition and equation (89) thus applies directly.

It is natural to suggest that an additional effect, caused by the quantum fluctuations of the amplitudes of Kelvin waves, will take place at low temperatures $T < T^*$. This quantum effect can be estimated by using the standard relation for the energy of the fundamental level of a harmonic oscillator $\Delta E = \hbar\omega(k)/2$. Applied to the Kelvin waves, this relation yields the k -independent quantum amplitude $A_Q^2 = m/4\pi^2 R \rho$. The quantum effect can thus be estimated as the sum

$$\sum_{N=\mathcal{N}_{\text{Kelvin}}^{\text{eq}}}^{\mathcal{N}_{\text{Kelvin}}} \frac{A_Q^2 N^2}{R^2} \sim \frac{A_Q^2 \mathcal{N}_{\text{Kelvin}}^3}{3R^2} = \frac{2m\pi}{3\rho\xi^3} = \frac{64\pi^{5/2}}{3\sqrt{2}} \left(\frac{\tilde{a}}{\ell}\right)^{3/2}. \quad (93)$$

The total effect is obtained superposing the thermal effect and the quantum effect and the final result is

$$\frac{\Delta v_L}{u_i} \Big|_{T < T^*} = \frac{64\pi^{5/2}}{3\sqrt{2}} \left(\frac{\tilde{a}}{\ell}\right)^{3/2} + \frac{(4/\sqrt{\pi})}{\zeta(\frac{3}{2}) C[\frac{R}{\xi}]^{3/2}} \left(\frac{T}{T_\lambda}\right)^{3/2} \quad (94)$$

$$\frac{\Delta v_L}{u_i} \Big|_{T > T^*} = \frac{8\sqrt{2\pi}}{\zeta(\frac{3}{2})^{2/3} C[\frac{R}{\xi}]} \left(\frac{\tilde{a}}{\ell}\right)^{1/2} \frac{T}{T_\lambda} \quad (95)$$

where $C[R/\xi] = \log(\frac{8R}{\xi}) - a$.

In the case of superfluid Helium, where $\tilde{a} \sim \ell$, the GPE description is only expected to give qualitative predictions and, at best, order of magnitude estimates (see ref.⁴). It is thus difficult to extend the above considerations, obtained in the case of weakly interacting BEC with $\tilde{a} \ll \ell$, to Helium.

Nevertheless the results obtained above in the weakly interacting case strongly suggest the presence of new slowing down effects, not included in the usual mutual friction descriptions of Helium that predicts $\frac{\Delta v_L}{u_i} \sim \rho_n/\rho \sim (T/T_\lambda)^4$. The new effects, because of their temperature dependence (see eq. (95)), should be dominant at low-temperature.

The zero-temperature quantum slowdown is independent of the ring diameter and the finite temperature effects are stronger for small rings. Time of flight measurements of vortex rings in ⁴He could be used to determine the translational velocity. The effect could also be studied in ultra-cold atomic gases BEC. For these systems the effect of the inhomogeneity of the superfluid should be taken into account⁵⁹.

VI. CONCLUSIONS

In summary our main results were obtained by making use of a stochastically forced Ginzburg-Landau equation (SGLE) that allowed us to efficiently obtain and control truncated Gross-Pitaevskii absolute equilibrium. This allowed us to show that the condensation transition observed in references^{13,24,25} corresponds to a standard second-order transition described by the $\lambda - \phi^4$ theory.

We also found that thermodynamic equilibrium can be obtained by a direct energy cascade, in a way similar to that of Cichowlas et al.¹⁸, accompanied by vortex annihilation as a prelude to final thermalization. Increasing the amount of dispersion of the system a slowdown of the energy transfer was produced inducing a partial thermalization independently of the truncation wavenumber.

Using the SGLE in the presence of a counterflow we observed that the counterflow can block the contraction of vortex rings reported by Berloff and Youd²⁷ and also induce a dilatation. We directly measured the mutual friction coefficient related to the transverse force. An unexpected result was found by immersing a vortex ring in a finite-temperature bath: a strong dependence of the translational velocity in the temperature was observed. This effect was an order of magnitude above the transverse mutual friction effect. We explained this effect by relating it to the anomalous translational velocity due to finite amplitude Kelvin waves that was previously found by Kiknadze and Mamaladze⁵⁶ and Barenghi et al.⁵⁷. Assuming equipartition of the energy of the Kelvin waves with the heat bath yields a formula that gives a very good quantitative estimate of the numerically observed effect. This new formula also gives an experimentally-testable quantitative prediction for the thermal slowdown of vortex rings in weakly interacting Bose-Einstein condensates and superfluid ⁴He.

The TGPE dynamics was thus found to contain many physically sound phenomenon of finite-temperature superflows. This strongly suggests the possibility to obtain the propagation of second sound waves in the TGPE. Some preliminary results support this conjecture (data not shown), however very high resolutions seem to be needed and this will be the subject of a future work.

Acknowledgments

We acknowledge useful scientific discussions with G. Düring and S. Rica. The computations were carried out at IDRIS (CNRS).

Appendix A: Conservation Laws and Dealiasing

In the standard case, for quadratic nonlinearities and quadratic invariants, the system can be correctly dealiased using the 2/3–rule that consists in truncation for wavenumber $|\mathbf{k}| < k_{\max} = N/3$, where $N/2$ is the

largest wavenumber of the discrete system. With this procedure, one third of the available modes are not used. Such discrete dealiased pseudo-spectral system exactly conserve the quadratic invariant and is therefore identical to the original Galerkin truncated system.

In the TGPE case, the problem is more complicated because the equation is cubic and the invariants are quartic. Let us first recall Parseval's theorem that states $\int d^3x f(\mathbf{x})g^*(\mathbf{x}) = V \sum_{\mathbf{k}} \hat{f}_{\mathbf{k}} \hat{g}_{\mathbf{k}}^*$, where $\hat{f}_{\mathbf{k}}$ and $\hat{g}_{\mathbf{k}}$ are the Fourier transform of f and g . This identity remains valid in truncated systems and it holds whether the functions are dealiased or not. The integration by parts formula is a consequence of Parseval's theorem:

$$\int d^3x f \frac{\partial g^*}{\partial x_j} = V \sum_{\mathbf{k}} -ik_j \hat{f}_{\mathbf{k}} \hat{g}_{\mathbf{k}}^* = - \int d^3x \frac{\partial f}{\partial x_j} g^*.$$

Remark that the product rule $(fg)' = f'g + fg'$ is only valid if the fields are dealiased.

The conservation of the total number of particles is directly obtained using the GPE (1)

$$\frac{dN}{dt} = \int d^3x (\dot{\psi}\bar{\psi} + \psi\dot{\bar{\psi}}) = \frac{i\hbar}{2m} \int d^3x (\bar{\psi}\nabla^2\psi - \psi\nabla^2\bar{\psi}) = 0.$$

where the last equality is a consequence of the Parseval identity and is thus true independently of dealiasing. Similar relations lead to the conservation of the energy H .

Using the dealiased TGPE (17) the conservation law for the momentum reads

$$\frac{dP_j}{dt} = 2g \int d^3x [(\partial_j \mathcal{P}_G[|\psi|^2]) |\psi|^2 + \mathcal{P}_G[|\psi|^2] \partial_j |\psi|^2]. \quad (\text{A1})$$

If ψ is dealiased the 2/3–rule implies that

$$\begin{aligned} \int d^3x (\mathcal{P}_G[|\psi|^2] \bar{\psi}) \partial_j \psi &= \int d^3x \mathcal{P}_G [\mathcal{P}_G[|\psi|^2] \bar{\psi}] \partial_j \psi \\ \partial_j (\mathcal{P}_G[|\psi|^2] \bar{\psi}) &= (\partial_j \mathcal{P}_G[|\psi|^2]) \bar{\psi} + \mathcal{P}_G[|\psi|^2] \partial_j \bar{\psi} \\ \partial_j |\psi|^2 &= \psi \partial_j \bar{\psi} + \bar{\psi} \partial_j \psi, \end{aligned}$$

it follows that $\frac{dP_j}{dt} = 0$. Without a Galerkin projector in eq. (17) the aliased field would obey $(|\psi|^2 \bar{\psi}) \partial_j \psi + (|\psi|^2 \bar{\psi}) \partial_j \bar{\psi} \neq \partial_j (|\psi|^4)$ and the conservation of momentum would therefore be lost.

Conservation of N , H and \mathbf{P} can be numerically checked by using absolute equilibria with non-zero momentum. The conservation of \mathbf{P} is ensured only if the system is dealiased. The error of aliased runs grow up to a 50% in a few units of time and is independent of the time-step (data not shown). We thus believe that it would be important to explicitly check the conservation of momentum when using finite-difference schemes, even if they exactly conserve the energy and the particle number.

Appendix B: Low-temperature calculation of thermodynamic functions

We are interested in computing the grand partition function \mathcal{Z} in eq.(46) where $F = H - \mu N - \mathbf{W} \cdot \mathbf{P}$ is written in terms of Fourier amplitudes as

$$\frac{H}{V} = \sum_{\mathbf{k}} \frac{\hbar^2 k^2}{2m} |A_{\mathbf{k}}|^2 + \frac{g}{2} \sum A_{\mathbf{k}_3+\mathbf{k}_1}^* A_{\mathbf{k}_2} A_{\mathbf{k}_4+\mathbf{k}_2}^* \delta_{\mathbf{k}_3, -\mathbf{k}_4} \quad (\text{B1})$$

$$N = V \sum_{\mathbf{k}} |A_{\mathbf{k}}|^2 \quad (\text{B2})$$

$$P_j = \sum_{\mathbf{k}} \hbar k_j |A_{\mathbf{k}}|^2 V \quad (\text{B3})$$

where $A_{\mathbf{k}} = 0$ if $k \geq k_{\max}$ and the second sum in H is over $\mathbf{k}_1, \mathbf{k}_2, \mathbf{k}_3, \mathbf{k}_4$.

The saddle-point is determined by the condition $\frac{\partial F}{\partial A_{\mathbf{k}}^*} - \mu_0 A_0 V \delta_{\mathbf{k},0} = 0$ which, explicitly written for $\mathbf{k} = \mathbf{0}$ and $\mathbf{k} \neq \mathbf{0}$, reads

$$(g|A_0|^2 - \mu + \mu_0)A_0 + 2g \sum_{\mathbf{k}_1 \neq \mathbf{0}} A_0 |A_{\mathbf{k}_1}|^2 + g \sum_{\mathbf{k}_1, \mathbf{k}_2 \neq \mathbf{0}} A_{\mathbf{k}_1} A_{\mathbf{k}_2 - \mathbf{k}_1}^* A_{-\mathbf{k}_2} = 0 \quad (\text{B4})$$

$$\frac{\hbar^2 k^2}{2m} A_{\mathbf{k}} - \mu A_{\mathbf{k}} - \hbar \mathbf{W} \cdot \mathbf{k} A_{\mathbf{k}} + g \sum_{\mathbf{k}_1, \mathbf{k}_2 \neq \mathbf{0}} A_{\mathbf{k}_1} A_{\mathbf{k}_2 + \mathbf{k}_1}^* A_{\mathbf{k} + \mathbf{k}_2} = 0 \quad (\text{B5})$$

from which eq.(47) follows.

To diagonalize $F = H - \mu N - \mathbf{W} \cdot \mathbf{P}$ we first apply the Bogoliubov transformation to $H - \mu N$ and then show that P is also diagonal in this basis. Replacing $B_{\mathbf{p}}$, defined by the transformation (51), in $H - \mu N$ (recall that $\mathbf{p} = \hbar \mathbf{k}$) and then imposing the diagonalization determines the coefficient L_p :

$$L_p = \frac{-2|A_0|^2 g - \frac{p^2}{2m} + \mu + \epsilon(p)}{|A_0|^2 g} \quad (\text{B6})$$

where $\epsilon(p)$ is given by

$$\epsilon(p) = \sqrt{\left(2|A_0|^2 g + \frac{p^2}{2m} - \mu\right)^2 - |A_0|^4 g^2}. \quad (\text{B7})$$

The dispersion relation (53) is obtained by replacing $|A_0|^2$ by its saddle-point value eq.(47).

We now express \mathbf{P} in the Bogoliubov base. Using (51) directly yields

$$|A_{\mathbf{p}}|^2 = |u_p|^2 |B_{\mathbf{p}}|^2 + |v_p|^2 |B_{-\mathbf{p}}|^2 + (u_p^* v_p^* B_{\mathbf{p}} B_{-\mathbf{p}} + c.c.). \quad (\text{B8})$$

Replacing eq.(B8) in the definition of \mathbf{P} (B3), the last two terms vanish by symmetry and using the relation $|u_p|^2 - |v_p|^2 = 1$, the momentum (B3) reads $\mathbf{P} = \sum_{\mathbf{p}} \mathbf{p} |B_{\mathbf{p}}|^2 V$. Gathering $H - \mu N$ and $\mathbf{W} \cdot \mathbf{P}$ formula (52) is finally obtained.

The mean value of the condensate amplitude is obtained as $V \overline{|A_0|^2} = - \frac{\partial \Omega}{\partial \mu_0} \Big|_{\mu_0=0}$. All the thermodynamic variables are directly generated by first putting $\mu_0 = 0$ in (58) and then by differentiation using relation (31). The fluctuations of the number of particles are computed as $\overline{\delta N^2} = -\beta^{-1} \frac{\partial^2 \Omega}{\partial \mu^2}$. These quantities are explicitly listed below.

$$\begin{aligned} \overline{|A_0|^2} &= \frac{\mu}{g} - \frac{\mathcal{N}}{V\beta\mu} f_0 \left[\frac{4m\mu}{P_{\max}^2} \right] \\ \bar{p} &= \frac{\mu^2}{2g} + \frac{\mathcal{N}}{V\beta} \left(\frac{2}{3} - f \left[\frac{4m\mu}{P_{\max}^2} \right] + \frac{2}{3} \frac{2w^2 m^2}{P_{\max}^2} f' \left[\frac{4m\mu}{P_{\max}^2} \right] \right) \\ \bar{N} &= \frac{V\mu}{g} - \frac{\mathcal{N}}{\beta} \left(\frac{3}{2\mu} f \left[\frac{4m\mu}{P_{\max}^2} \right] - \frac{8w^2 m^3}{P_{\max}^4} f_2 \left[\frac{4m\mu}{P_{\max}^2} \right] \right) \\ S &= \mathcal{N} \left(f \left[\frac{4m\mu}{P_{\max}^2} \right] \left(1 + \frac{2w^2 m}{4\mu} \right) - \log \left[\frac{\beta \epsilon(P_{\max}; \mu)}{e^{-\frac{5}{3}}} \right] \right) \\ \lambda_{\mathcal{N}} &= \beta^{-1} \log [\beta \epsilon(P_{\max}; \mu)] - \frac{1}{3\beta} \frac{2w^2 m^2}{P_{\max}^2} \frac{1}{1 + \frac{4m\mu}{P_{\max}^2}} \\ \bar{P}_z &= \frac{\mathcal{N}}{\beta} \frac{wm}{\mu} f \left[\frac{4m\mu}{P_{\max}^2} \right] + \frac{3\mathcal{N}}{10\beta} \frac{w^3 m^2}{\mu^2} f_1 \left[\frac{4m\mu}{P_{\max}^2} \right] \\ \overline{\delta N^2} &= \frac{V}{g\beta} + \frac{3\mathcal{N}}{4\beta^2 \mu^2} f_1 \left[\frac{4m\mu}{P_{\max}^2} \right], \end{aligned} \quad (\text{B9})$$

$$f[z] = z - z^{3/2} \cot^{-1}(\sqrt{z}) \quad (\text{B10})$$

$$f_0[z] = 3(z + 3f[z])/4 \quad (\text{B11})$$

$$f_1[z] = \frac{z}{z+1} - f(z) \quad (\text{B12})$$

$$f_2[z] = \frac{d}{dz}(f[z]/z) \quad (\text{B13})$$

The dependence of the entropy on the phase-space normalization constant is manifested by the presence of the logarithm term in S and $\lambda_{\mathcal{N}}$. Note that the function $S + \beta \lambda_{\mathcal{N}}$ is, however, completely defined. Also note that the pressure p must be computed, by definition, at constant total number of modes \mathcal{N} . All the thermodynamic relations discussed in section IIB can be explicitly checked on the low-temperature expressions. The previous formulae have been confronted with the SGLE numerically generated data in Fig.2.a-b.

- ¹ L. D. Landau and L. M. Lifshitz. *Course of Theoretical Physics, Volume VI: Fluid Mechanics*. Butterworth-Heinemann, 2 edition, January 1987.
- ² W. F. Vinen. Mutual Friction in a Heat Current in Liquid Helium II. III. Theory of the Mutual Friction. *Proceedings of the Royal Society of London. Series A. Mathematical and Physical Sciences*, 242(1231):493–515, 1957.
- ³ Nick P Proukakis and Brian Jackson. Finite-temperature models of Bose–Einstein condensation. *J. Phys. B: At. Mol. Opt. Phys.*, 41(20):203002, Oct 2008.
- ⁴ R. J. Donnelly. *Quantized Vortices in Helium II*. Cambridge Univ. Press, 1991.
- ⁵ C Nore, M Abid, and ME Brachet. Kolmogorov turbulence in low-temperature superflows. *Physical Review Letters*, 78(20):3896–3899, Jan 1997.
- ⁶ C Nore, M Abid, and ME Brachet. Decaying Kolmogorov turbulence in a model of superflow. *Phys. Fluids*, 9(9):2644–2669, Jan 1997.
- ⁷ M Kobayashi and M Tsubota. Kolmogorov spectrum of superfluid turbulence: Numerical analysis of the Gross-Pitaevskii equation with a small-scale dissipation. *Physical Review Letters*, 94(6):065302, Jan 2005.
- ⁸ Jeffrey Yepez, George Vahala, Linda Vahala, and Min Soe. Superfluid turbulence from quantum Kelvin wave to classical Kolmogorov cascades. *Physical Review Letters*, 103(8):084501, Aug 2009.
- ⁹ M Abid, ME Brachet, J Maurer, C Nore, and P Tabeling. Experimental and numerical investigations of low-temperature superfluid turbulence. *Eur J Mech B-Fluid*, 17(4):665–675, Jan 1998.
- ¹⁰ J Maurer and P Tabeling. Local investigation of superfluid turbulence. *Europhysics Letters*, 43(1):29–34, Jan 1998.
- ¹¹ G. P. Bewley, M. S. Paoletti, K. R. Sreenivasan, and D. P. Lathrop. Characterization of reconnecting vortices in superfluid helium. *PNAS*, 105(37):13707–13710, 2008.
- ¹² M. S. Paoletti, M. E. Fisher, K. R. Sreenivasan, and D. P. Lathrop. Velocity statistics distinguish quantum turbulence from classical turbulence. *Physical Review Letters*, 101(15):154501, 2008.
- ¹³ MJ Davis, SA Morgan, and K Burnett. Simulations of Bose fields at finite temperature. *Physical Review Letters*, 87(16):160402–160402, 2001.
- ¹⁴ T.D. Lee. On some statistical properties of hydrodynamical and magneto-hydrodynamical fields. *Quart Appl Math*, 10(1):69–74, Jan 1952.
- ¹⁵ R. Kraichnan. On the statistical mechanics of an adiabatically compressible fluid. *J Acoust Soc Am*, 27(3):438–441, Jan 1955.
- ¹⁶ R. Kraichnan. Helical turbulence and absolute equilibrium. *Journal of Fluid Mechanics*, 59(AUG7):745–752, Jan 1973.
- ¹⁷ S.A. Orszag. *Statistical Theory of Turbulence*. in, Les Houches 1973: Fluid dynamics, R. Balian and J.L. Peube eds. Gordon and Breach, New York, 1977.
- ¹⁸ C Cichowlas, P Bonaiti, F Debbasch, and M Brachet. Effective dissipation and turbulence in spectrally truncated Euler flows. *Physical Review Letters*, 95(26):264502, Jan 2005.
- ¹⁹ W. J. T Bos and J.P. Bertoglio. Dynamics of spectrally truncated inviscid turbulence. *Phys. Fluids*, 18(7):071701, Jan 2006.
- ²⁰ G Krstulovic and M Brachet. Two-fluid model of the truncated Euler equations. *Physica D: Nonlinear Phenomena*, 237(14-17):2015–2019, Aug 2008.
- ²¹ G Krstulovic, P D Mininni, M E Brachet, and A Pouquet. Cascades, thermalization, and eddy viscosity in helical Galerkin truncated Euler flows. *Physical review. E*, pages 1–5, May 2009.
- ²² Uriel Frisch, Susan Kurien, Rahul Pandit, Walter Pauls, Samridhi Sankar Ray, Achim Wirth, and Jian-Zhou Zhu. Hyperviscosity, Galerkin truncation, and bottlenecks in turbulence. *Physical Review Letters*, 101(14):144501, Jan 2008.
- ²³ G. Krstulovic, C. Cartes, M. Brachet, and E. Tirapegui. Generation and characterization of absolute equilibrium of compressible flows. *International Journal of Bifurcation and Chaos (IJBC)*, 19(10):3445–3459, 2009.
- ²⁴ C Connaughton, C Josserand, A Picozzi, Y Pomeau, and S Rica. Condensation of classical nonlinear waves. *Physical Review Letters*, 95(26):263901, Jan 2005.
- ²⁵ Antonio Picozzi Gustavo Düring and Sergio Rica. Breakdown of weak-turbulence and nonlinear wave condensation,. *Physica D*, 238(16):1524–1549, August 2009.
- ²⁶ NG Berloff and BV Svistunov. Scenario of strongly nonequilibrated Bose-Einstein condensation. *Physical Review A*, 66(1):013603, Jan 2002.
- ²⁷ Natalia G Berloff and Anthony J Youd. Dissipative dynamics of superfluid vortices at nonzero temperatures. *Physical Review Letters*, 99(14):4, Oct 2007.
- ²⁸ Jean Zinn-Justin. *Phase Transitions and Renormalisation Group*. Oxford University Press, USA, August 2007.
- ²⁹ Daniel J. Amit and Victor Martin-Mayor. *Field Theory; The Renormalization Group and Critical Phenomena*. World Scientific Publishing Company, June 2005.
- ³⁰ M Abid, C Huepe, S Metens, C Nore, CT Pham, LS Tuckerman, and ME BRACHET. Gross-Pitaevskii dynamics of Bose-Einstein condensates and superfluid turbulence. *Fluid Dyn Res*, 33(5-6):509–544, Jan 2003.
- ³¹ D. Gottlieb and S. A. Orszag. *Numerical Analysis of Spectral Methods*. SIAM, Philadelphia, 1977.
- ³² L. D. Landau and L. M. Lifshitz. *Course of Theoretical Physics, Volume V: Statistical Physics (Part 1)*. Butterworth-Heinemann, August 1996.
- ³³ N. G. van. Kampen. *Stochastic processes in physics and chemistry / N.G. van Kampen*. North-Holland ; sole distributors for the USA and Canada, Elsevier North-Holland, Amsterdam ; New York : New York :, 1981.
- ³⁴ Flor Langouche, Dirk Roekaerts, and Enrique Tirapegui. *Functional integration and semiclassical expansions*. D Reidel Pub Co, Jan 1982.
- ³⁵ Jon Mathews and Robert Lee Walker. *Mathematical methods of physics*. W. A. Benjamin, 1970, Jan 1970.
- ³⁶ E. M. Lifshitz and L. P. Pitaevskii. *Course of Theoretical Physics, Volume IX: Statistical Physics (Part 2)*. Butterworth-Heinemann, January 1980.
- ³⁷ J Lipa, J Nissen, D Stricker, and D Swanson. Specific heat of liquid helium in zero gravity very near the lambda point. *Phys. Rev. B*, Jan 2003.
- ³⁸ Giorgio Krstulovic and Marc Brachet. Comment on “Superfluid turbulence from quantum Kelvin wave to classical Kolmogorov cascades”. *Phys. Rev. Lett.*, 105(12):129401, Sep 2010.
- ³⁹ E Fermi, J Pasta, and S Ulam. Studies of nonlinear prob-

- lems. *LASL Report LA-1940*, Jan 1955.
- ⁴⁰ E. A. L Henn, J. A Seman, G Roati, K. M. F Magalhaes, and V. S Bagnato. Emergence of turbulence in an oscillating Bose-Einstein condensate. *Physical Review Letters*, 103(4):045301, Jan 2009.
- ⁴¹ Giorgio Krstulovic and Marc Brachet. Dispersive bottleneck delaying thermalization of turbulent Bose-Einstein condensates. *arXiv*, physics.flu-dyn, Jul 2010.
- ⁴² C Huepe, S Metens, G Dewel, P Borckmans, and ME Brachet. Decay rates in attractive Bose-Einstein condensates. *Physical Review Letters*, 82(8):1616–1619, Jan 1999.
- ⁴³ C. W. Gardiner. *Handbook of Stochastic Methods: For Physics, Chemistry and the Natural Sciences (Springer Series in Synergetics)*. Springer, November 1996.
- ⁴⁴ T Winiecki, JF McCann, and CS Adams. Vortex structures in dilute quantum fluids. *Europhysics Letters*, 48(5):475–481, Jan 1999.
- ⁴⁵ C Huepe and ME Brachet. Scaling laws for vortical nucleation solutions in a model of superflow. *PHYSICA D-NONLINEAR PHENOMENA*, 140(1-2):126–140, JUN 1 2000.
- ⁴⁶ Tuckerman LS, Huepe C, and Brachet ME. Numerical methods for bifurcation problems. 9:75–83, 2004.
- ⁴⁷ CT Pham, C Nore, and ME Brachet. Boundary layers and emitted excitations in nonlinear Schrödinger superflow past a disk. *PHYSICA D-NONLINEAR PHENOMENA*, 210(3-4):203–226, OCT 15 2005.
- ⁴⁸ C Nore, ME Brachet, E Cerda, and E Tirapegui. Scattering of first sound by superfluid vortices. *Physical Review Letters*, 72(16):2593–2595, Jan 1994.
- ⁴⁹ DJ Thouless, P Ao, and Q Niu. Transverse force on a quantized vortex in a superfluid. *Physical Review Letters*, 76(20):3758–3761, Jan 1996.
- ⁵⁰ GE Volovik. Transverse force on a quantized vortex in a superfluid - comment. *Physical Review Letters*, 77(22):4687–4687, Jan 1996.
- ⁵¹ C Wexler. Magnus and Iordanskii forces in superfluids. *Physical Review Letters*, 79(7):1321–1324, Jan 1997.
- ⁵² HE Hall and JR Hook. Comment on "Magnus and Iordanskii forces in superfluids". *Physical Review Letters*, 80(19):4356–4356, Jan 1998.
- ⁵³ EB Sonin. Comment on "Berry's phase and the magnus force for a vortex line in a superconductor," "transverse force on a quantized vortex in a superfluid," and "Magnus and Iordanskii forces in superfluids". *Physical Review Letters*, 81(19):4276–4276, Jan 1998.
- ⁵⁴ C Wexler, DJ Thouless, P Ao, and Q Niu. Comment on "Magnus and Iordanskii forces in superfluids" - Wexler et al reply. *Physical Review Letters*, 80(19):4357–4357, Jan 1998.
- ⁵⁵ J Fuchs, G Malka, J. C Adam, F Amiranoff, S. D Baton, N Blanchot, A Héron, G Laval, J. L Miquel, P Mora, H Pépin, and C Rousseaux. Fuchs et al. reply:. *Physical Review Letters*, 81:4275, Nov 1998.
- ⁵⁶ L Kiknadze and Y Mamaladze. The waves on the vortex ring in heii. *Journal of Low Temperature Physics*, 126(1-2):321–326, Jan 2002.
- ⁵⁷ C. F Barengi, R Hanninen, and M Tsubota. Anomalous translational velocity of vortex ring with finite-amplitude Kelvin waves. *Physical Review E*, 74(4):046303, Jan 2006.
- ⁵⁸ CF Barengi, RJ Donnelly, and WF Vinen. Thermal excitation of waves on quantized vortices. *Phys Fluids*, 28(2):498–504, Jan 1985.
- ⁵⁹ Giorgio Krstulovic and Marc Brachet. Anomalous vortex ring velocities induced by thermally-excited Kelvin waves and counterflow effects in superfluids. *arXiv*, cond-mat.stat-mech, Jun 2010.
- ⁶⁰ VA Zagrebnov and JB Bru. The Bogoliubov model of weakly imperfect Bose gas. *Phys Rep*, 350(5-6):292–434, Jan 2001.
- ⁶¹ The Galilean invariant expression of \mathbf{W} is $\mathbf{V}_n - \mathbf{V}_s$ (see sec.V)
- ⁶² Grand canonical computations avoid difficulties that are present in the canonical ensemble with the explicit conservation of the number of particles (see section 2.2 of reference⁶⁰ and references therein)
- ⁶³ The thermodynamic limit is taken over the grand canonical potential $\Omega = -\beta^{-1} \log \mathcal{Z}$ as $V \left(\lim_{V \rightarrow \infty} \frac{\Omega}{V} \right)$.
- ⁶⁴ <http://www.vapor.ucar.edu>